# AN ULTRASONIC INVESTIGATION OF STATIC AND DYNAMIC CRITICAL EFFECTS IN THE MIXED JAHN-TELLER SYSTEM $DyAs_xV_{1-x}O_4$

By

HUSSEIN MOHAMED ELMEHDI

A thesis submitted to the Faculty of Graduate Studies as
a requirement for the degree of
Master of Science

DEPARTMENT OF PHYSICS
UNIVERSITY OF MANITOBA
WINNINPEG, MANITOBA, CANADA
R3T 2N2

MAY 1991

© Copyright by Hussein Mohamed Elmehdi, 1991.

National Library of Canada
Bibliothèque nationale du Canada

Canadian Theses Service
Service des thèses canadiennes

Ottawa, Canada
K1A 0N4

The author has granted an irrevocable non-exclusive licence allowing the National Library of Canada to reproduce, loan, distribute or sell copies of his/her thesis by any means and in any form or format, making this thesis available to interested persons.

The author retains ownership of the copyright in his/her thesis. Neither the thesis nor substantial extracts from it may be printed or otherwise reproduced without his/her permission.

L'auteur a accordé une licence irrévocable et non exclusive permettant à la Bibliothèque nationale du Canada de reproduire, prêter, distribuer ou vendre des copies de sa thèse de quelque manière et sous quelque forme que ce soit pour mettre des exemplaires de cette thèse à la disposition des personnes intéressées.

L'auteur conserve la propriété du droit d'auteur qui protège sa thèse. Ni la thèse ni des extraits substantiels de celle-ci ne doivent être imprimés ou autrement reproduits sans son autorisation.

ISBN 0-315-76823-1

Canada

# AN ULTRASONIC INVESTIGATION OF STATIC AND DYNAMIC CRITICAL EFFECTS IN THE MIXED JAHN TELLER SYSTEM $DyAs_xV_{1-x}O_4$

BY

HUSSEIN MOHAMED ELMEHDI

A thesis submitted to the Faculty of Graduate Studies of the University of Manitoba in partial fulfillment of the requirements of the degree of

MASTER OF SCIENCE

© 1991

Permission has been granted to the LIBRARY OF THE UNIVERSITY OF MANITOBA to lend or sell copies of this thesis. to the NATIONAL LIBRARY OF CANADA to microfilm this thesis and to lend or sell copies of the film, and UNIVERSITY MICROFILMS to publish an abstract of this thesis.

The author reserves other publication rights, and neither the thesis nor extensive extracts from it may be printed or otherwise reproduced without the author's written permission.

In the name of God, the Beneficent, the Merciful

**ABSTRACT**

Ultrasonic velocity measurements were performed in the frequency range 11 MHz to 120 MHz to investigate the dynamic and static critical effects due to random fields at the structural phase transitions in the mixed Jahn-Teller compounds $DyAs_xV_{1-x}O_4$. Elastic constant, ($c=\rho v^2$), was investigated for two samples having strong random fields ( $x = 0.164$; $T/T_D = 0.38$ and $T/T_D = 0.42$) and a third sample with weaker random fields ($x = 0.154$; $T/T_D = 0.54$).

For the samples with strong random fields, dynamic rounding of the soft-mode elastic constant ($\propto 1/\chi$ near the critical region) was observed, indicating extreme slowing down of critical fluctuations due to the random fields. Although clear evidence of dynamic rounding of the phase transition was shown, data over a wider range of frequencies is needed to determine whether the data is properly described by an activated model as proposed by Villain (1985) and Fisher (1986) for random-field systems, or by conventional dynamic scaling.

For the sample with weaker random fields ($x = 0.154$), the soft mode elastic constant was found to be independent of the ultrasonic frequency in the range 11 MHz to 70 MHz, implying that static critical behavior is not obscured by dynamic effects and enabling the susceptibility exponent to be measured. We found that $\gamma=1.78\pm0.07$, which is consistent with several theoretical predictions and previous experiments on this compound (Graham *et al.* (1991)).

## ACKNOWLEDGEMENTS

I would like to thank my advisor J.H. Page for providing assistance and showing extreme patience throughout the course of this work.

I would like to thank all the St.Vital guys *(especially the married ones )* for their dinner parties, the M.S.A brothers, my body building partner Fawzi for pushing me to the limit, and my soccer and hockey buddies for all the great games.

Special thanks to my brothers Elmehdi, Othman, and Hadi for keeping me updated with all the family affairs back home.

Thanks also go to Jim Graham, Gilles Roy, and Jim Gould for all the help they provided. Finally I would also like to thank Hank and Norbert for being my lab mates.

To: Ali Bin Mehdi

## Contents


Page

**Chapter One: Introduction** ..... 1

**Thesis Outline** ..... 5

**Chapter Two: Theory** ..... 6

**2.1 Introduction** ..... 7

**2.2 Jahn-Teller Effect** ..... 7

2.2.1 Introduction ..... 7
2.2.2 The Jahn-Teller Hamiltonian of the Dy System ..... 8

**2.3 Molecular Field solution** ..... 13

**2.4 Relation to Elastic Constants** ..... 16

**2.5 Mixed Jahn-Teller compound $DyAs_xV_{1-x}O_4$** ..... 21

2.5.1 Random Field Ising Model ..... 21
2.5.2 Dynamic Effects Near Phase Transition ..... 24

**Chapter Three: Experimental Techniques** ..... 26

**3.1 A Brief Discussion of the Pulse Echo Technique** ..... 27

**3.2 Measurements of the Ultrasonic Velocity Change as a Function of Temperature** ..... 29

3.2.1 Phase Cancellation Method ..... 29
3.2.2 Signal Averaging ..... 33

**3.3 Room Temperature Absolute Velocity Measurements** ..... 35

**3.4 Sample Polishing** ..... 40

**3.5 Sample Bonding** ..... 41

**3.6 Coaxial Delay Cables Corrections** ..... 42

3.6.1 Introduction ..... 42
3.6.2 Method ..... 43

**Chapter Four: Results and Discussion** ..... 47

**4.1 Data Collection and Analysis** ..... 48

4.1.1 Quartz Delay Correction ..... 48
4.1.2 Indium Correction ..... 50
4.1.3 Sample Delay ..... 52
4.1.4 The Ultrasonic Velocity ..... 52

**4.2 Determination of Elastic Constants** ..... 56

**4.3 Dynamic Critical Behavior** ..... 62

**4.4 Static Critical Behavior** ..... 77

**Chapter Five Conclusions** ..... 90

**Appendix I**

Determination of Longitudinal and Shear Velocities of Indium ..... 93

**Appendix II** Sample Misalignment Correction ..... 97

**References** ..... 100

# CHAPTER ONE: INTRODUCTION

Both of the rare earth compounds dysprosium arsenate ($DyAsO_4$) and dysprosium vanadate ($DyVO_4$) undergo structural phase transitions which are caused by the co-operative Jahn-Teller effect (CJTE). This type of phase transition is driven by a linear coupling between the lattice displacements and the electronic states of the rare earth ions ( Elliott *et al* (1972) ). For $DyAsO_4$ and $DyVO_4$ the crystallographic symmetry is lowered from the tetragonal zircon structure ( space group $D_{4h}^{19}$ ) to an orthorhombic structure ( space group $D_{2h}^{28}$), resulting in an increase in the separation of the lowest electronic levels of $Dy^{3+}$, thereby lowering the electronic energy at low temperatures. Earlier experiments ( *eg.* see Kaston (1980), Page *et al* (1984) ) showed that the phase transitions in $DyAsO_4$ and $DyVO_4$ occur at transition temperature $T_D$ of 11.4 K and 14.6 K respectively. The order of the transition in the two compounds is different: first order (*discontinous*) in $DyAsO_4$, and second order (*continuous*) in $DyVO_4$.

Mixing the two compounds $DyVO_4$ and $DyAsO_4$ has the effect of introducing random strains which are caused by the different unit cell sizes of the two compounds. Previous experiments have suggested that the mixed compounds $DyAs_xV_{1-x}O_4$ provide a good experimental system for studying the Random-Field Ising Model (RFIM) problem, since (i) the interactions between the rare-earth ions that cause the phase transition are well described by a pseudo-spin Ising Hamiltonian, (ii) the

interactions are ferrodistortive, (iii) large static random strain fields can be generated via the coupling to lattice strains, (iv) there is no dilution of the ion-ion interactions as the concentration x is varied, unlike the diluted antiferromagnetic compounds used to study the random-field problem, and (v) the interactions have a large short-range component (which in pure $DyVO_4$ determines the observed critical behavior in the accessible range of temperatures near the transition ) so that the nearest-neighbor interactions assumed in the RFIM should provide a good description of $DyAs_xV_{1-x}O_4$. The RFIM has been of considerable interest recently due to theoretical predictions of new critical behaviour and slow equilibration near and below $T_c$ which leads to metastability and hysteresis ( for a review, see Jaccarino and King (1988)).

Previous experiments done on $DyAs_xV_{1-x}O_4$ (Page *et al.* (1988) and Graham *et al.* (1991) ) to investigate the critical behavior have shown that the transition temperature $T_D$ depends strongly on the arsenic concentration x. The phase transition was also found to be more rounded in the random systems, an effect that was attributed to modified critical behavior in which the susceptibility critical exponent was increased dramatically from 1.15±.05 to 1.79±0.07 by the random fields. Other possible contributions to the rounding of the phase transition could be: i) concentration inhomogeneities, which cause the distortion temperature to be different at different regions of the sample, and ii)

dynamic non-equilibrium effects due to extreme slowing down of critical fluctuations near the transition temperature. The effect of concentration inhomogeneities was investigated by Graham *et al.* (1991) and found to be too small to significantly affect the rounding of the transition. Dynamic effects on the rounding of the phase transition have been predicted by Villain (1985) and Fisher (1986). The only experimental evidence of such effects is that of Jaccarino *et al.* (1991), who used AC susceptibility measurements on the dilute anti-ferromagnet $Fe_{0.46}Zn_{0.54}F_2$ over a wide range of frequencies. They found that the rounding of the phase transition was indeed affected by dynamic effects and could be interpreted in terms of the activated model proposed by Villain and Fisher.

The main aim of this work is to look for evidence of such dynamic effects in the Jahn-Teller system $DyAs_xV_{1-x}O_4$. Three samples of different random field strengths (x=0.164, and x=0.154) were studied. To investigate the critical dynamics and their possible contribution to the rounding of the phase transition, the elastic constant $c_{11}$ was measured for the three samples as a function of temperature over as wide a range of frequency as could be realized with the available apparatus.

## THESIS OUTLINE

Chapter two presents the theory behind the structural phase transition. A brief introduction to the Jahn-Teller structural phase transition is given and the Hamiltonian of the system is derived, with its molecular field solution. The elastic constants and their relation to the susceptibility are then derived thermodynamically. The final section in chapter two deals with random fields in the mixed Jahn-Teller compounds $DyAs_xV_{1-x}O_4$.

Chapter three explains the experimental methods, including the measurements of the ultrasonic velocity as a function of temperature (this was required to determine the elastic constant *i.e.* $c=\rho v^2$, where $\rho$ is the sample density and v is the ultrasonic velocity). A description of the equipment used for these measurements, with related block diagrams, are also given. Sample bonding and polishing are also treated in this chapter.

Data collection, analysis, and the results of all the experiments are included in chapter four, along with a discussion of the results. Finally the conclusions are stated in chapter five.

# CHAPTER TWO :THEORY

## 2.1 INTRODUCTION

In this chapter a brief introduction is given to structural phase transitions driven by the Jahn-Teller effect. A detailed theory of the Co-operative Jahn-Teller phase transition is presented, including a molecular field solution of the Hamiltonian of the system. The behavior of the soft-mode elastic constant near the phase transition is derived thermodynamically . The next section deals with the mixed Jahn-Teller compounds $DyAs_xV_{1-x}O_4$ where the random-field effects arising from mixing $DyAsO_4$ and $DyVO_4$ are discussed. Finally a discussion of the susceptibility critical exponent and dynamic effects associated with the phase transition are also presented .

## 2.2 JAHN-TELLER EFFECT ( JTE )

### 2.2.1 INTRODUCTION

The Jahn-Teller structural phase transition is driven by the interaction between degenerate electron states localized on a particular ion and a lattice distortion. As a result, the symmetry of the electronic states is lowered and the degeneracy is removed, so that the energy of one of the electronic states is lowered while the other is raised. If the lower state is preferentially occupied , the electronic energy will decrease by an amount that Jahn and Teller (1937) showed

would be proportional to the distortion. In addition there will be an increase in the elastic energy that is quadratic in the distortion. The result is that an equilibrium situation is attained for a finite distortion which minimizes the total energy. For example, if there is a local distortion, measured by $\zeta$, of the crystallographic environment around the ion, the total energy $E(\zeta)$ can be written as

$$E(\zeta) = -a\zeta + b\zeta^2$$

where a and b are constants. The minimum then occurs at

$$\zeta_0 = a/2b \ ,$$

and the minimum energy is lowered to the value

$$E(\zeta_0) = E_{JT} = -a^2/4b.$$

## 2.2.2. THE JAHN-TELLER HAMILTONIAN OF THE Dy-SYSTEM

The Hamiltonian can be found by writing the distortion $\zeta$ in terms of the normal modes of the crystal. To avoid the problem of applying periodic boundary conditions to the distorting crystal, we separate the lattice modes into two categories: uniform strains and phonons. The uniform strains are treated first and periodic boundary conditions are then applied to the strained crystal in calculating the phonon

contribution. A uniform local strain $e_\Gamma$ is defined as ( see for example, Nye (1957))

$$e_\Gamma = e_{ij} = \frac{1}{2}\left( \frac{\partial u_i}{\partial x_j} + \frac{\partial u_j}{\partial x_i} \right) , (i,j = x,y,z) \ldots\ldots\ldots (2.2.1)$$

where $\Gamma$ represents the strain symmetry and $\mathbf{u}$ is the lattice displacement caused by the strain.

The long-wavelength acoustic phonons may be treated as local fluctuations in the strain, so that the displacements $\mathbf{u}$ are now given by,

$$u_i = 1/\sqrt{N}\Sigma_{\mathbf{k}} Q(\mathbf{k})\ p_i(\mathbf{k}) \exp[i\ \mathbf{k}.\mathbf{R}_n] \ldots\ldots\ldots\ldots\ldots (2.2.2)$$

Here $Q(\mathbf{k})$ is the normal mode coordinate at wave vector k, and $p_i(\mathbf{k})$ is the polarization vector. $Q(\mathbf{k})$ is defined in terms of the annihilation and creation operators $a_{\mathbf{k}}$ , $a^+_{\mathbf{k}}$ as follows

$$Q(\mathbf{k}) = [\hbar/2M\omega(\mathbf{k})]^{1/2} \left( a^+_{\mathbf{k}} + a_{-\mathbf{k}} \right) \ldots\ldots\ldots\ldots (2.2.3)$$

For simplicity we restrict our discussion to phonons of a single branch, so the branch index can be omitted.

We first discuss the coupling between the electronic states and the bulk strain mode, since it is convenient to treat this contribution to the lattice displacements separately from the phonon contributions. The Hamiltonian of a system with a strain $e_\Gamma$ is (Gehring and Gehring 1975),

$$\mathcal{H}_s = \sum_n R_s\, e_\Gamma O_\Gamma(n) + 2\, N\, V_0 c_\Gamma^0 e_\Gamma^2 \qquad (2.2.4)$$

where $R_s$ is the coupling constant, $e_\Gamma$ is the strain, $O_\Gamma(n)$ is the operator representing the electronic states, N is the number of unit cells, $V_0$ is the unit cell volume, and $c_\Gamma^0$ is the unperturbed elastic constant . Minimizing the Hamiltonian with respect to the variable $e_\Gamma$ gives the equilibrium value

$$e_\Gamma = (1/NV_0 c_\Gamma^0) \Sigma_n R_s O_\Gamma(n) \qquad (2.2.5)$$

at the minimum. Substituting (2.2.5 ) in (2.2.4) the Hamiltonian of the system becomes

$$\mathcal{H} = -\frac{\mu}{2N} \Sigma_{n,m} \sigma^z(n)\, \sigma^z(m) \qquad (2.2.6)$$

where $\mu = \dfrac{R_s^2}{4V_0 c_\Gamma^0}$, and the electronic operators $O_\Gamma(n)$ representing the two energy levels are written as pseudo-spin operators $\sigma^z(n)$ having

eigenvalues $\mp 1$. Here the strain coupling now gives rise to an infinite ranged interaction between the magnetic $Dy^{3+}$ ions represented by the pseudo-spin operators.

The Hamiltonian that describes the coupling between the electronic states and the acoustic phonons is found by substituting (2.2.2) and (2.2.3) for the phonon displacements into (2.2.1) and (2.2.4), giving

$$\mathcal{H}_s = \sum_k \hbar\,\omega(\mathbf{k})\ \left( a^+(\mathbf{k})a(\mathbf{k}) + \frac{1}{2} \right) + \sum_k \xi(\mathbf{k})[a(-\mathbf{k})^+ + a(\mathbf{k})\ ]\ \sigma^z(\mathbf{k}) \ldots \quad (2.2.7)$$

where $$\xi(\mathbf{k}) = R_s \left( \frac{i}{2} \right) \left\{ \frac{\hbar}{2MN\omega(\mathbf{k})} \right\}^{1/2} \{k_i p_j(\mathbf{k}) + k_j p_i(\mathbf{k})\ \}\ ,$$

is the coupling strength constant, and

$$\sigma^z(k) = \frac{1}{N^{1/2}} \sum_n \sigma^z(n)\ \exp[i(\mathbf{k}.\mathbf{R}(n))]$$

The coupling to the optic phonons has the same form as (2.2.7). This Hamiltonian can be simplified by introducing the displaced operators $\gamma^+(k)$ and $\gamma(k)$ which define the excitations relative to the local distortions ,where

$$\gamma^+(\mathbf{k}) = [a^+(\mathbf{k}) + \frac{\xi(\mathbf{k})}{\hbar\omega(\mathbf{k})}\ \sigma_{\mathbf{k}}\ ]\ , \text{ and}$$

$$\gamma\ (\mathbf{k}) = [\ a(\mathbf{k}) + \frac{\xi(\mathbf{k})}{\hbar\omega(\mathbf{k})}\sigma_{-\mathbf{k}}]\ .$$

Note that the commutation relation $[a^{+}(\mathbf{k}),a(\mathbf{k}')]= [\gamma^{+}(\mathbf{k}),\gamma(\mathbf{k}')\ ] = \delta_{\mathbf{k},\mathbf{k}'}$ still holds. Substituting the displaced operators into equation (2.2.7), the Hamiltonian in (2.2.7) becomes

$$\mathcal{H}= \sum_{\mathbf{k}}\ \hbar\omega(\mathbf{k})\ [\gamma^{+}(\mathbf{k})\ \gamma(\mathbf{k}) + \frac{1}{2}\ ] - \sum_{\mathbf{k}}\ \frac{|\xi(\mathbf{k})|^2}{\hbar\omega(\mathbf{k})}\ \sigma(\mathbf{k})\ \sigma(-\mathbf{k})\ .....(2.2.8)$$

Thus the Jahn-Teller coupling gives rise to an effective interaction between the $Dy^{3+}$ ions which is of the Ising form. The strength of the ion-ion coupling is conveniently written in terms of the effective exchange constant $J(\mathbf{k})$ which is defined by

$$J\ (\mathbf{k}) = \frac{2|\xi(\mathbf{k})|^2}{\hbar\omega(\mathbf{k})} - \frac{1}{N}\ \Sigma\ \frac{2|\xi\ (\mathbf{k})\ |^2}{\hbar\omega(\mathbf{k})}$$

with its Fourier Transform

$$J\ (\mathbf{n},\mathbf{n}') = (1-\delta_{\mathbf{n},\mathbf{n}'})\ \sum_{\mathbf{k}}\ \frac{2\xi(\mathbf{k})}{\hbar\omega(\mathbf{k})}\ \exp[\ i\mathbf{k}\ .(\ \mathbf{R}(\mathbf{n})- \mathbf{R}(\mathbf{n}')\ )$$

which defines the ion-ion interaction at positions n,n'. The n = n' term is called the self energy and must be subtracted from the ion-ion effective interaction which is given by

$$- \frac{1}{2} \sum_{n,n'} J(n,n') \sigma^z(n) \sigma^z(n').$$

For the dysprosium compounds investigated in this thesis, the electronic states are not exactly degenerate in the absence of the Jahn-Teller interaction, but are split by an amount $2\varepsilon$ due to the crystalline electric field. The total Hamiltonian which includes this crystal field is term then (Elliott *et al.* (1972) )

$$\mathcal{H} = \sum_{\mathbf{k}} \hbar\omega(\mathbf{k}) [\gamma(\mathbf{k}) \gamma^+(\mathbf{k}) + \frac{1}{2}] - \frac{1}{2} \sum_{n,n'} [J(n,n') + \frac{\mu}{N}] \sigma^z(n)\sigma^z(n') - \varepsilon \sum_n \sigma^x(n). \quad \text{.....(2.2.10)}$$

This Hamiltonian has the form of an Ising model in a transverse field.

## 2.3 MOLECULAR FIELD SOLUTION

Molecular field theory (MFT) describes an approximation for studying a system of interacting spins in which the effect of all neighboring spins on a representative spin is described by their thermal average. Thus each spin experiences an effective field which is proportional to the magnetization.

In the molecular field approximation, the Hamiltonian of the system

becomes

$$\mathcal{H}_{m.f} = -(\lambda+\mu)\ \langle\sigma^z\rangle \sum_n \sigma_n^z - \varepsilon \sum_n \sigma_n^x, \quad \ldots\ldots\ldots\ldots\ldots\ldots\ldots\ldots (2.3.1)$$

where $\lambda = \sum_n J(n,m) = J(0)$ and $\langle\sigma^z\rangle$ is the thermal average. Diagonalizing the Hamiltonian, the energy levels are given by $\mp W$ where

$$W = \{ [( \lambda + \mu)\langle\sigma^z\rangle]^2 + \varepsilon^2\}^{1/2}$$

Now the average values of $\sigma^z$ and $\sigma^x$ are found by projecting the total pseudo-spin average value $\langle\sigma\rangle$, where

$$\langle\sigma\rangle = \tanh\left(\frac{W}{k_B T}\right),$$

along the x and z axes to give

$$\langle\sigma^z\rangle = \cos\theta\tanh(W/k_B T), \text{and}$$

$$\langle\sigma^x\rangle = \sin\theta\tanh(W/k_B T).$$

Here $\theta$ is rotational angle in the pseudo-spin xz-plane,

$$\tan\theta = \frac{\varepsilon}{(\lambda+\mu)\langle\sigma^z\rangle} \quad \ldots\ldots\ldots\ldots\ldots\ldots\ldots (2.3.2)$$

In this approximation, the phase transition occurs at a temperature $T_D=(\lambda+\mu)/\langle\sigma^z\rangle$ below which $\langle\sigma^z\rangle$ is no longer zero. In the distorted phase $T<T_D$, the expressions for W, $\langle\sigma^z\rangle$, and $\langle\sigma^x\rangle$ can be written as

$$W=(\lambda+\mu)\tanh(W/k_BT)$$

$$\langle\sigma^z\rangle= (W^2+\varepsilon^2)/(\lambda+\mu).$$

$$\langle\sigma^x\rangle=\varepsilon/(\lambda+\mu).$$

In the undistorted phase, $T>T_D$, we have,

$$W=\varepsilon$$

$\langle\sigma^z\rangle=0$, giving

$$\langle\sigma^x\rangle= \tanh(\varepsilon/k_BT).$$

If the high temperature splitting is negligible ($\varepsilon\rightarrow 0$) these expressions will be simplified to give

$$W = (\lambda+\mu)\langle\sigma^z\rangle$$

$$\langle \sigma^x \rangle = 0$$

$$\langle \sigma^z \rangle = \tanh(W/k_B T).$$

Above $T_D$, $\langle \sigma^x \rangle = 0$, $\langle \sigma^z \rangle = 0$, and $W = 0$.

## 2.4 RELATION TO ELASTIC CONSTANTS

For the Dy compounds under investigation, the order parameter in the JT distortion is proportional to the lattice strain $B_{1g}$. This macroscopic strain of $B_{1g}$ symmetry corresponds to a stretch along the x-axis and an equal compression along the y-axis giving the symmetrized strain

$$e_{B1g} = e_{xx} - e_{yy},$$

where $e_{ij}$ is defined in (2.2.1). For a review of elastic constants see for example Nye (1957). The coupling between the strain and the rare earth ions is given by the term $- R_S e_{B1g} \sigma^z$, $R_S$ being the coupling constant.

For the tensor strain $e_{B1g}$ as defined above, the strain elastic energy is ( Elliott *et al.* (1972), Gehring and Gehring (1975)),

$$U = \frac{1}{4} NV_0 ( c_{11} - c_{12} ) ( e_{B1g} )^2 \quad \ldots\ldots\ldots\ldots (2.4.1)$$

N is the number of unit cells, and $V_0$ is the unit cell volume.

The behavior of the elastic constant $\frac{1}{2}(c_{11}-c_{12})$ can be obtained from the Helmholtz free energy as follows. The Helmholtz free-energy, $F = \langle \mathcal{H} \rangle - TS$ is equal to

$$-2Nk_B T \ln [2 \cosh(W/kT)] + N\lambda \langle \sigma^z \rangle^2 + \frac{1}{4} NV_0 (c_{11} - c_{12}) e^2 \ldots . (2.4.2)$$

where W now is written as

$$W = [ ( \lambda \langle \sigma^z \rangle + R_s e)^2 + \varepsilon^2 ]^{1/2},$$

to show the dependence on strain $e$ explicitly. $\lambda \langle \sigma^z \rangle^2$ is the molecular field self energy in the unit cell, and the $B_{1g}$ subscript is dropped. The condition $\partial F / \partial \langle \sigma^z \rangle = 0$ determines the equilibrium value of $\langle \sigma^z \rangle$, and gives the same result as in the previous section.

The stress in the mode $B_{1g}$ is defined as,

$$\mathcal{T}_0 = \frac{1}{V N} \left( \frac{\partial F}{\partial e} \right)_0 = \frac{-2 R_s \langle \sigma^z \rangle}{V} + \frac{1}{2} (c_{11} - c_{12}) e \quad \ldots\ldots\ldots (2.4.3)$$

Setting $\mathcal{T} = 0$ gives the equilibrium value of the strain as

$$\langle e \rangle = \frac{4R_s \langle \sigma^z \rangle}{V_0 (c_{11} - c_{12})} \quad \ldots\ldots\ldots\ldots\ldots\ldots (2.4.5)$$

The elastic constant $c_\vartheta$ with $B_{1g}$ symmetry is defined by

$$c_\vartheta = (\partial \mathcal{F} / \partial e)_\vartheta ,$$

where $\vartheta$ denotes the thermodynamic measurement condition. Using (2.4.3), this gives

$$c_\vartheta = \frac{-2\eta}{V_0} \left( \frac{\partial \langle \sigma^z \rangle}{\partial e} \right)_\vartheta + c_0 \quad \ldots\ldots\ldots\ldots\ldots\ldots (2.4.6)$$

where $c_0$ is the unperturbed value of $\frac{1}{2}(c_{11}-c_{12})$.

$c_\vartheta$ can be conveniently written in terms of the single-ion susceptibility $g_\vartheta$ which is defined as

$$g_\vartheta = \left( \frac{\partial \langle \sigma^z \rangle}{\partial \mathcal{H}_e} \right).$$

Here $\mathcal{H}_e = J(0) \langle \sigma^z \rangle + R_s e$ is the effective molecular field acting on the $\sigma^z$ operators. Using the relation

$$\left( \frac{\partial \langle \sigma^z \rangle}{\partial e} \right)_\vartheta = \left( \frac{\partial \langle \sigma^z \rangle}{\partial \mathcal{H}_e} \right)_\vartheta \left( \frac{\partial \mathcal{H}_e}{\partial e} \right)_\vartheta$$

$$= g_\vartheta \left[ \lambda \left( \frac{\partial \langle \sigma^z \rangle}{\partial e} \right)_\vartheta + R_s \right],$$

gives the result

$$\left( \frac{\partial \langle \sigma^z \rangle}{\partial e} \right)_{\vartheta} = \frac{R_s g_{\vartheta}}{1 - \lambda g_{\vartheta}}.$$

Thus we obtain the general expression

$$\frac{c_{\vartheta}}{c_0} = \frac{1 - (\lambda+\mu) g_{\vartheta}}{1 - \lambda g_{\vartheta}} \quad \ldots\ldots\ldots\ldots\ldots\ldots (2.4.7)$$

Since ultrasonic measurements are done adiabatically, we only consider the adiabatic *"perfectly isolated"* susceptibility. Here the spin populations are kept constant when changing the strain, which is equivalent to keeping $\langle\sigma\rangle = \tanh(W/k_B T)$ constant and allowing only the angle $\theta$ in equation (2.3.2) to vary. In this case $g_{\vartheta} = g_s$ which is given by

$$g_s = \varepsilon \langle \sigma^z \rangle / W^2.$$

Substituting this expression into (2.4.7) we get

$$\frac{c_s}{c_0} = \frac{(\lambda+\mu)^2 \langle \sigma^z \rangle^2 + \varepsilon(\varepsilon - (\lambda+\mu)\langle \sigma^x \rangle)}{(\lambda+\mu)^2 \langle \sigma^z \rangle^2 + \varepsilon(\varepsilon - \lambda \langle \sigma^x \rangle)} \quad \ldots\ldots\ldots (2.4.8)$$

This expression can be simplified if we consider $T > T_D$ where $\langle\sigma^z\rangle = 0$, giving

$$\frac{c_s}{c_0} = \frac{\varepsilon - (\lambda+\mu)\langle\sigma^x\rangle}{\varepsilon - \lambda\langle\sigma^x\rangle} .$$

At $T = T_D$, $\langle\sigma^z\rangle$ is still zero but $\langle\sigma^x\rangle = \varepsilon/(\lambda+\mu)$, so $c_s$ goes continuously to zero as $T_D$ is approached from above.

The elastic constant can be expressed in terms of the total pseudo-spin susceptibility which is defined as

$$\chi = \lim_{\mathcal{T}\to 0} \left( \frac{c_0}{R_s N} \frac{\partial\langle\sigma^z\rangle}{\partial\mathcal{T}} \right), \quad \ldots\ldots\ldots\ldots\ldots\ldots (2.4.9)$$

and which measures the response of the $\langle\sigma^z\rangle$ operators to an external stress. $\chi$ is the analog for the JT phase transition to the magnetic susceptibility at a ferromagnetic phase transition. In the presence of a stress $\mathcal{T}$ the electronic energy in the Hamiltonian (2.2.4) is increased by $NVe\mathcal{T}$ and the equilibrium strain becomes (Page (1976) )

$$e = \frac{\mathcal{T}}{2c_0} + \frac{R_s}{4NV_0 c_0} \langle\sigma^z\rangle . \quad \ldots\ldots\ldots\ldots\ldots\ldots (2.4.10)$$

The elastic constant c then is given by

$$\frac{1}{c} = \lim_{\mathcal{J} \to 0} \left( 2 \frac{\partial e}{\partial \mathcal{J}} \right),$$

so that,

$$c = \frac{c_0}{1 + \mu\chi}$$

In the critical region near the phase transition temperature $T_D$, the susceptibility diverges as

$$\chi \propto t^{-\gamma}$$

Here $t=(T-T_D)/T_D$ is the reduced temperature, and $\gamma$ is the susceptibility critical exponent. Thus near the phase transition when $\chi \gg 1$,

$$\frac{1}{c} \propto t^{-\gamma}, \text{ or } c \propto t^{\gamma}. \quad \ldots\ldots\ldots\ldots\ldots\ldots\ldots (2.4.11)$$

## 2.5 MIXED JAHN-TELLER COMPOUND $DyAs_xV_{1-x}O_4$

### 2.5.1 RANDOM FIELD ISING MODEL(RFIM)

Mixing the two compounds $DyAsO_4$ and $DyVO_4$ has the effect of inducing random strains which are due to the different unit cell sizes of the two compounds. One component of this random strain field will have the right symmetry to couple to the electronic levels . The

Hamiltonian (2.3.1) is modified by adding a new term which results from this coupling,

$$\mathcal{H} = \mathcal{H}_{Ising} + \mathcal{H}_{R.F}$$

$$= \sum_{i,j} J_{ij}\sigma_i^z\sigma_j^z + \sum_i h_i\sigma_i^z$$

where $h_i$ is the random strain field, which depends on the arsenic concentration $x$. Note here that $J_{ij}$ does not depend on the concentration $x$. This modified Hamiltonian shows that the mixed compounds $DyAs_xV_{1-x}O_4$ are a structural counterpart to a ferromagnet in a random magnetic field, and as such they are expected to be an interesting experimental realization of the random-field Ising model.

In the pure $DyVO_4$, even though the critical behavior is ultimately classical sufficiently close to $T_D$, the critical behavior that is observable in the experimentally accessible range of temperatures near $T_D$ is influenced by the short-range interactions, and the measured exponents compare to those of the nearest-neighbor Ising model ( Harley and MacFarlane (1975) ). Thus it is reasonable to expect that the critical behavior of the mixed compounds will be influenced by the random fields and provide a good experimental test of the nearest-neighbor Random Field Ising Model. Some additional advantages of this system are: a) Unlike diluted antiferromagnets in a uniform field which are believed to be equivalent to the random-field ferromagnet,

$DyAs_xV_{1-x}O_4$ presents no dilution problem (Huse and Henley 1985), since the interactions in this mixed system are between the $Dy^{3+}$ ions and their concentration is unaffected by mixing. b) It is possible to study the response of the system to an applied ordering field which can be varied by changing the applied stress. A drawback of this system is that the random field is fixed in the sample, so that the only way to vary the random field is by changing the sample.

This RFIM has been of considerable interest recently due to theoretical predictions of new critical behavior and slow equilibration near and below $T_c$ which leads to metastability and hysteresis (Jaccarino (1988)). There have been several mixed Jahn-Teller compounds for which some properties have been studied. In $Tm_xLu_{1-x}VO_4$ the specific heat was measured by Gehring *et al.* (1976). Phase transitions in the $Tb_xGd_{1-x}VO_4$ antiferromagnet were studied by Glynn *et al.* (1977), who showed that this system undergoes a double phase transition. Kaston *et al.* (1984) and Taylor *et al.*(1986) studied the phase transition concentration dependence for $Tb_xTm_{1-x}AsO_4$. However all of these diluted Jahn-Teller compounds are dominated by long-range interactions and are expected to show different critical properties to the mixed $DyAs_xV_{1-x}O_4$ system studied in this thesis. In random-field magnets, there have been very few experimental studies of the critical exponents, the only measurement of $\gamma$ being that of Belanger *et al.* (1985). They investigated the d=3 diluted antiferromagnet $Fe_{0.6}Zn_{0.4}F_2$ using neutron

scattering and obtained a value for $\gamma$ of 1.75±0.2, although their result has been viewed with caution because of the lack of a rigorous theory for the neutron-scattering line shape on which their value of $\gamma$ depends.

There have been several relevant theoretical predictions for modified critical behavior in random field Ising systems. Aharony *et al.* (1976) predicted that the critical exponents for the d-dimensional (2<d<4) system with short-range exchange and random fields are the same as the (d-1)-dimension pure system, leading to a value for $\gamma$ of 1.75. Another prediction is presented by Ogielski and Huse (1986) using a Monte Carlo simulation of the 3-d dilute antiferromagnet in a uniform field, their value for $\gamma$ being 2.0 ± 0.5. We finally mention the work of Bray and Moore (1985) who developed a scaling theory for the Random Ising Model in 2+$\varepsilon$ dimension which gave $\gamma = (3-d+1.5)/\varepsilon$, implying for three dimensions that $\gamma$ = 1.5 ($\varepsilon$=1).

## 2.5.2 DYNAMIC EFFECTS NEAR THE PHASE TRANSITION

Villain *et al.* (1985) and Fisher (1986) predicted extreme slowing down of critical fluctuations near $T_c$ in a random field systems. In their models, the characteristic time $\tau$ for a fluctuation on a scale of the correlation length $\xi$ grows as

$$\tau \propto \exp ( \xi^{\Theta} ) \propto \exp ( C t^{-\nu\Theta} )$$

where $\Theta$ is a new exponent that governs the growth of the free energy in a volume $\xi^d$ and $\nu$ is the correlation length exponent ( $\xi \propto t^{-\nu}$ ). The basic idea is that the dynamics are determined by an activated process involving hopping over barriers induced by the random fields. Close to $T_D$, $\tau$ becomes very long because of this exponential dependence on $\xi$, leading to dynamic rounding at reduced temperatures $t<t^*(\omega)$, as non-equilibrium behavior sets in at frequency $\omega$. In terms of the elastic constant $c(\omega,t)$, Fisher's model for the susceptibility implies

$$c(\omega,t) \propto t^{\gamma} \cdot F\left(\frac{|\ln\omega/\omega_0|}{t^{-\Theta\nu}}\right)$$

where $\omega_0$ is some characteristic frequency and F is a universal scaling function. Thus the dynamic elastic constant no longer goes to zero at the transition but reaches a minimum value $c_{min}(\omega)$ at a reduced temperature $t_{min}(\omega)$ which can be greater than zero. These quantities scale with frequency as

$$c(\omega)_{min} \propto |\ln(\omega/\omega_0)|^{-\gamma/\nu\Theta} ,$$

$$t(\omega)_{min} \propto |\ln(\omega/\omega_0)|^{-1/\nu\Theta} .$$

In fact it is the main aim of the experiments reported in this thesis to see if such dynamics are important at ultrasonic frequencies in $DyV_xAs_{1-x}O_4$.

# CHAPTER 3 EXPERIMENTAL TECHNIQUES

In this chapter the experimental methods and equipment are discussed. The measurements of ultrasonic velocity using the pulse echo technique are done in two ways: the room temperature *"absolute"* velocity, and the velocity change as a function of temperature. These two procedures are discussed, including the techniques used to measure and control the sample temperature. Sample polishing and bonding are discussed briefly.

## 3.1 A BRIEF DISCUSSION OF THE PULSE ECHO TECHNIQUE

The basic idea of the pulse echo technique is to subject the specimen under investigation to a stress wave ( ultrasonic ) of a short pulse duration relative to the time $t_o$ for the pulse to travel one round trip in the sample ( for example, for shear ultrasonic waves propagating along the [100] direction in sample *A1*, the pulse width was 0.4 μsec, while $t_o$ was 3.637 μsec ). The direction in which the pulse is applied to the sample is perpendicular to sample parallel faces. An electromagnetic pulse is converted into an ultrasonic mechanical stress wave via a piezoelectric transducer. The transducer resonates at its fundamental frequency (given by the condition $f=v/2s'$, where f is the frequency, v is the sound velocity in the transducer and $s'$ is the transducer thickness ) and all odd harmonics; this determines the possible frequencies of operation. The transducer is bonded to a delay

rod which delays the ultrasonic signals to allow for separation between the reflected sample echoes and the non-converted initial electromagnetic pulse which is also detected by the receiver. The ultrasonic velocity is then determined from the measured transit time $t_0$ and the thickness of the sample $s$ ($v=2s/t_0$).

The ultrasonic wave generated by the transducer travels through the the delay rod and is partially reflected at the delay-rod/sample interface. The other part is transmitted into the sample and continues to travel until it reaches the sample-air interface at the far side of the sample, at which it is completely reflected back towards the transducer. The reflected signals arriving at the transducer are partly reflected back into the delay rod for another round trip while the other part is converted by the transducer into electric energy waves which are then amplified and displayed on an oscilloscope. Accurate timing measurements can then be performed on the sample echoes to determine the ultrasonic velocity, as described in detail in the next section.

## 3.2 MEASUREMENTS OF THE ULTRASONIC VELOCITY CHANGE AS A FUNCTION OF TEMPERATURE

### 3.2.1 PHASE CANCELLATION METHOD

In this method the change in ultrasonic velocity in the sample was measured as the temperature was varied from room temperature down to

liquid helium temperature ( *i.e* 295 to 4.2 K ). This was done in two stages, first the sample was cooled down to liquid nitrogen temperature ( 77 K ) and then subsequently cooled to 4.2 K (usually the next day).

The basic idea of the measurements is to superimpose a radio frequency ( RF ) generated reference signal pulse on the reflected sample signal, and to establish destructive interference between the two signals so that the phase of the sample signal can be determined. The phase and amplitude of the reference signal can be adjusted using a set of variable delay lines and an adjustable attenuator. The reference signal is coherent with the signal sent to the sample.

The apparatus was set up as shown in figure 3.1. The RF pulse used to generate the sample echoes is obtained by modulating the continuous wave output of a frequency synthesizer ( FLUKE 6060B ) with a square pulse from a pulse generator ( STANFORD RESEARCH SYSTEM , INC. MODEL D6535 ). The pulse generator is also used control the pulse width and time delay of the RF signal. The pulse width of the signal must be wide enough to allow for the finite rise and fall times of the transducer response but not too wide to cause interference between any two adjacent echoes. The first constraint on the pulse width enables a constant echo amplitude to be established in the interference region, while the second is required to eliminate spurious phase shifts due to echo overlap. The

modulation is done via a set of three mixers (MINI-CIRCUITS 15542 ) each of which reduces the CW background by 30dB relative to the RF signal. The signal is then amplified using a power amplifier which has a maximum output power of about 50W. The output signal is fed into a two stage diode expander which blocks the low amplitude noise but allows the high power pulses to pass virtually unattenuated. There is also a 3dB attenuator which isolates the amplifier from reflected signals, thereby improving its stability. Before reaching the transducer, the electromagnetic pulse passes through a double stub tuner ( WEINSCHEL ENGINEERING HS40 ) which provided a way of matching the impedance of the transducer to the impedance of the measuring system ( 50 Ohm ). One difficulty in using the double stub tuner is that it broadens the pulses, so that we were unable to use it for measurements in the thinnest sample for which pulses shorter than 200nsec were required. At the transducer the electromagnetic pulse is converted to an ultrasonic signal, which then travels through the delay rod and the sample where it is reflected back and forth, resulting in a train of echoes.

The retransduced signals are fed via a power splitter into precision attenuator (TELONIC MODEL 8143S and 8123S ) which can be set from 0.0 to 111.0 decibels to adjust the signal level. These echoes are then coupled to the reference signal at the directional coupler and amplified by the receiver ( MATEC MODEL 254 and KEITHLEY INSTRUMENTS MODEL 107 ), and finally viewed on the oscilloscope ( HEWLETT PACKARD

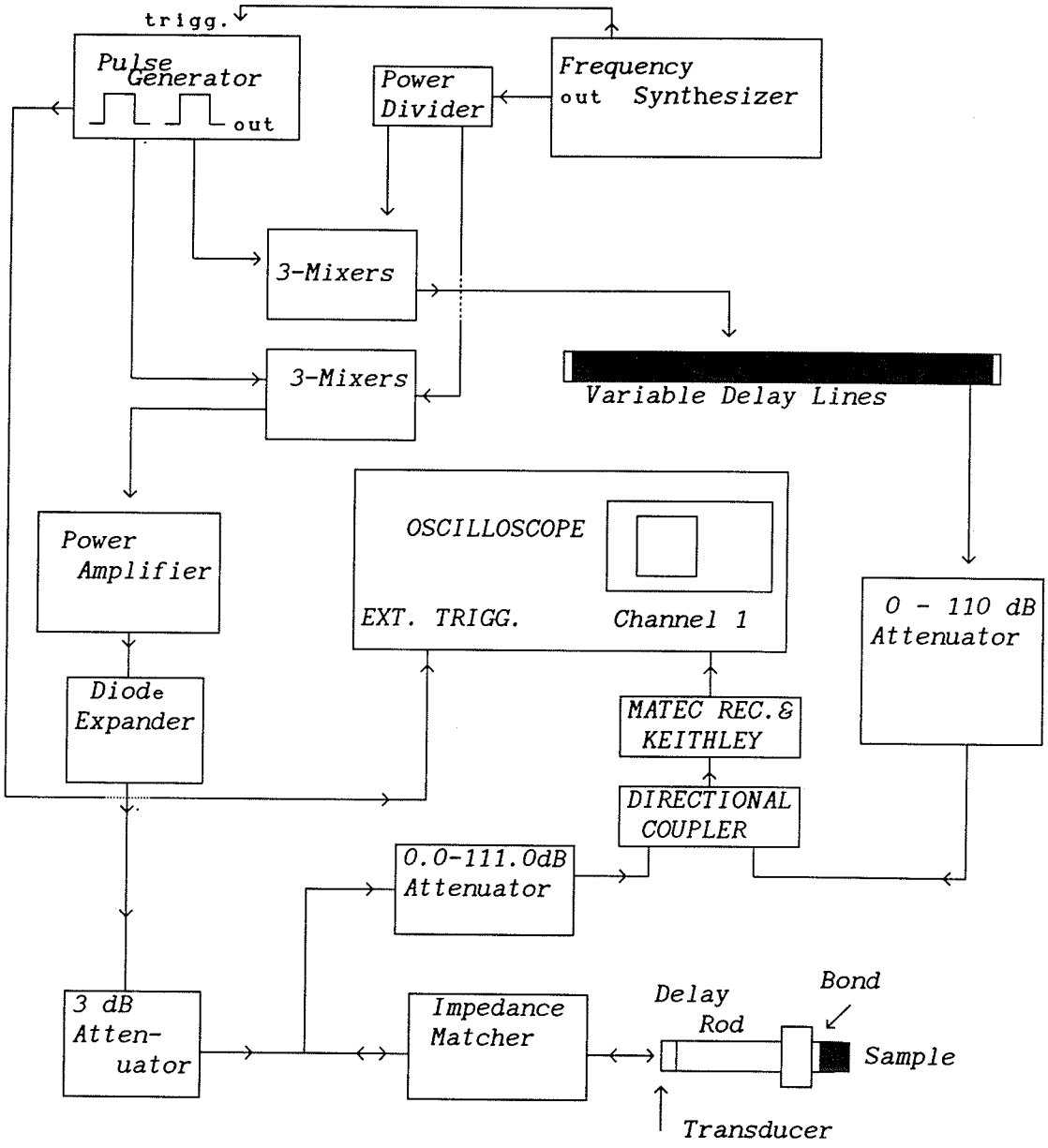


*FIGURE 3.1*
*BLOCK DIAGRAM FOR THE VELOCITY CHANGE MEASUREMENTS*

MODEL 1725A ). The oscilloscope is triggered externally by the pulse generator.

The reference signal is also obtained from the continuous wave signal from the Fluke frequency synthesizer so that it is coherent with the signal sent to the sample. A second square pulse originating from the Stanford pulse generator and a pair of (HP 141) mixers were used to amplitude modulate these continuous wave signals to create a long (about 10$\mu$sec) radio frequency pulse, timed to overlap the sample signal. The pulse is then phase shifted using air-filled continuously variable delay lines (0 to 250cm) and a set of coaxial cables which can be added in nine different lengths ( ranging from 39 cm to 1500 cm ) depending on the wavelength $\lambda$ used. The reference signal is then connected to an attenuator that can be adjusted from 0 to 110 dB in order to vary the level of the reference pulse to match that of the sample signal. Thus both the phase and amplitude of the reference signal could be adjusted to obtain null signals on the oscilloscope. Changes in the sample velocity could be accurately measured from the change in the phase of the reference needed to maintain a null. One of the sample echoes ( usually the first reflected sample echo ) was selected and the reference signal was superimposed on it by time delaying the reference signal ( this is done using the delay features of the pulse generator and had no effect on the phase of the reference signal). The cancellation region was taken to be at the peak of the reflected sample

echo, where the signal level is maximum so as to optimize the sensitivity.

The sample temperature was controlled by a Lake Shore Cryotronics controller which uses a carbon resistor as a feed back sensor and two calibrated thermometers, a silicon diode and a carbon glass resistor, to measure the temperature. For the low temperature measurements ( 77 K to 4.2 K ) we used the carbon glass resistor which was believed to give the more accurate calibration. Both thermometers were glued ( using G.E VARNISH ) as close to the sample as possible. The sample was placed in a cylindrical copper cell around which the heater coil was wrapped. The copper cell is hung inside two concentric stainless steel cans which were placed in the helium dewar. Helium exchange gas was added to the two stainless cans to insure good thermal contact between the sample, the heater, and thermometer without evaporating an unnecessary amount of liquid helium from the dewar.

### 3.2.2 SIGNAL AVERAGING TECHNIQUE

This method was used when the signal-to-noise ratio was so small that the phase cancellation method was not sufficiently accurate to make meaningful measurements. This problem arose in our experiments when the attenuation of the sample signal became very high at low temperatures near the phase transition.

In this method a high resolution Tektronix digital oscilloscope, borrowed from the electrical engineering department (DSA 600 series), was used to digitize part of the echo train with a timing resolution of 10ps, and to perform summation signal averaging on successive sweeps to dig the radio frequency sample signal out of the random background noise. One problem that occurred was that, after averaging, the background was found to contain a radio frequency component with the same frequency as the ultrasonic echo; this radio frequency background was separately digitized ( by taking advantage of the fact that below the transition temperature, ultrasonic attenuation in the sample was so high that the sample echo was completely suppressed ) and later subtracted from the measured signal to leave only the transduced ultrasonic signal from the sample. To effect this background subtraction, averaged signals were transferred using the RS232 interface to an IBM compatible 286 computer and analyzed using the ASYST software package.

The time delay was measured by fitting a straight line to the zero crossover region of an RF oscillation ( chosen from the middle of the stored signal ) and finding the intercept relative to the corresponding zero crossing at a reference temperature. Thus changes in the propagation time could be directly determined to a precision of about 20ps, providing that the sample signal was larger than the RF background signal. For smaller sample signals, the data was severely limited by

background noise and by small shifts in the continuous RF background component.

## 3.3 ROOM TEMPERATURE ABSOLUTE VELOCITY MEASUREMENTS

Measurements of the ultrasonic velocity at room temperature were done by measuring the time $t_0$ taken by the pulse to travel a round trip through the sample. The velocity is then determined by :

$$V = \frac{2s}{t_0},$$

where $s$ is the sample thickness. The equipment arrangement was similar to that of section ( 2.2.1 ) but with no reference signal as shown in figure 3.2. The time interval $t_0$ was measured using the $\Delta t$ option of the HP1724 oscilloscope which enabled the time to be directly read on a voltmeter ( FLUKE 8840 digital multimeter ). This was done by first dividing ( via a power divider ) the reflected train of echoes, after being received by the Matec receiver, into two signals and then feeding, with equal length cables, each of the signals into one channel of the oscilloscope. The oscilloscope was calibrated using the frequency synthesizer. The delay trigger on the oscilloscope was adjusted to overlap two of the sample echoes ( e.g. $S_{11}$ with $S_{12}$, see figure 3.3 ), the time interval $\Delta t$ being read on the digital voltmeter. The two echoes were accurately overlapped on the oscilloscope by adjusting the trigger

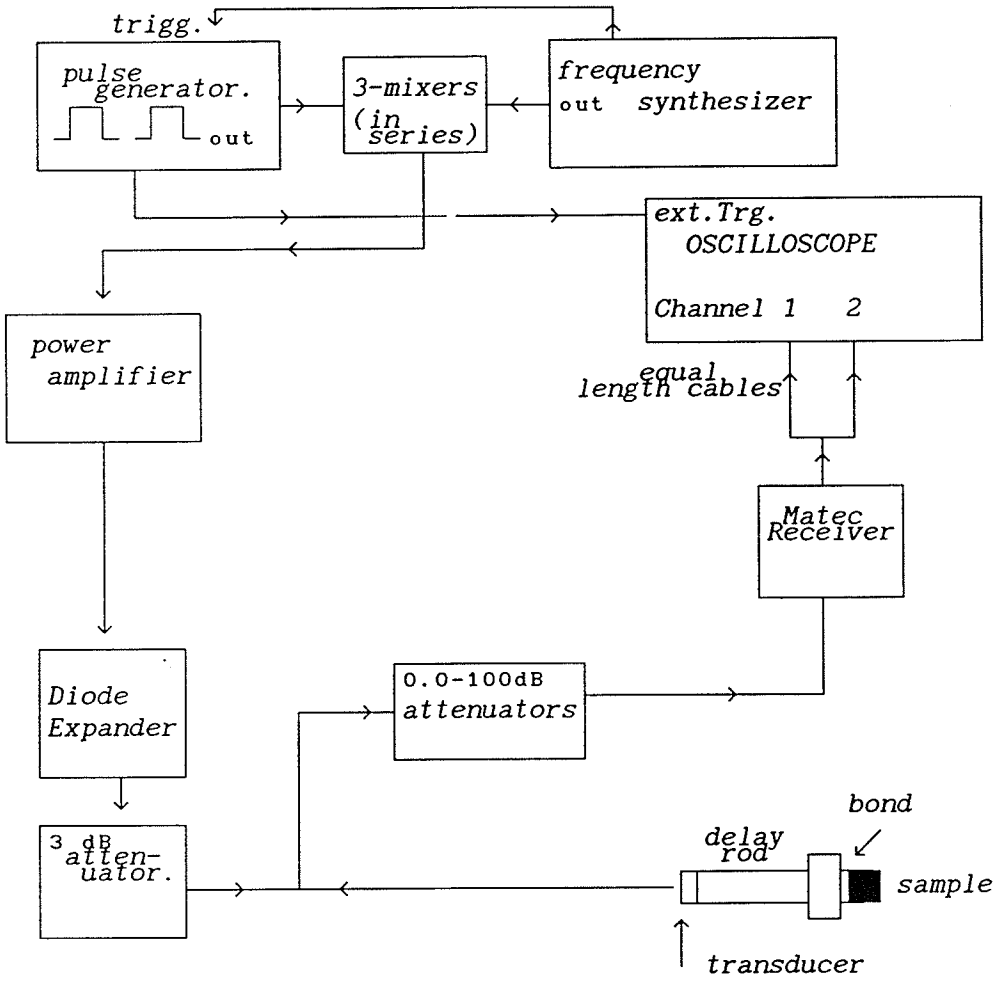


*FIGURE 3.2*
*THE ABSOLUTE VELOCITY MEASUREMENTS BLOCK DIAGRAM.*

delay to line up the RF oscillations in the two pulses. This was done for optimum alignment and also for -1 ,and +1 cycle permitting corrections to be made for phase shifts at the sample/delay-rod interface. This procedure was done for several frequencies ( no less than four ). The *"absolute"* time $t_0$ was then determined by extrapolating to the zero period $\tau$ ( $\tau = \frac{1}{f}$ , f is the frequency ) at which any phase shifts vanish. These linear fits to the data for $\Delta t$ verses $\tau$ meet at the the same point on the ordinate, which is the true time interval $t_0$. An example of such measurements is shown in figure 3.4. It should be noted here the temperature was kept constant throughout these measurements.

In later measurements this method was modified slightly , by using the Stanford pulse generator to delay trigger the oscilloscope after the HP oscilloscope became unstable. The A output of the pulse generator was used to trigger the oscilloscope so that the zero crossing of one of the RF oscillations of the first echo was centered on the screen. The B output was then adjusted to line up the appropriate zero crossing of the second echo on the screen, the time difference $\Delta t$ being read directly off the digital display of the pulse generator.

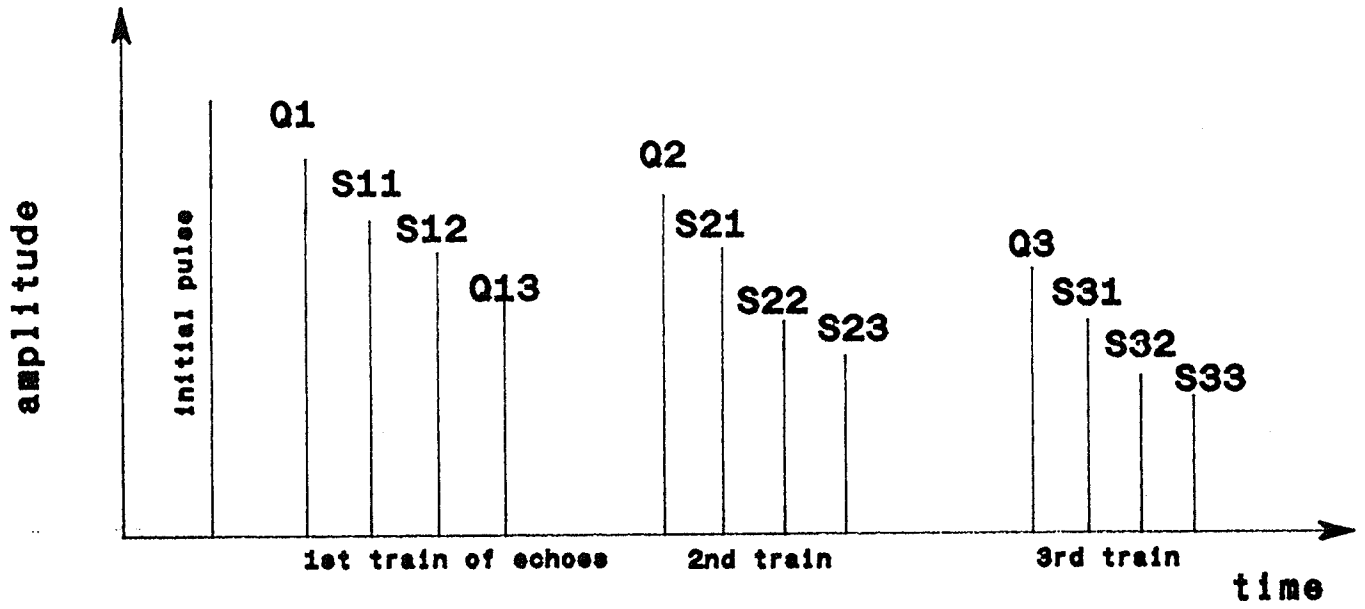


Figure 3.3 Observed Train of Echoes
{Q=Quartz and S= Sample}

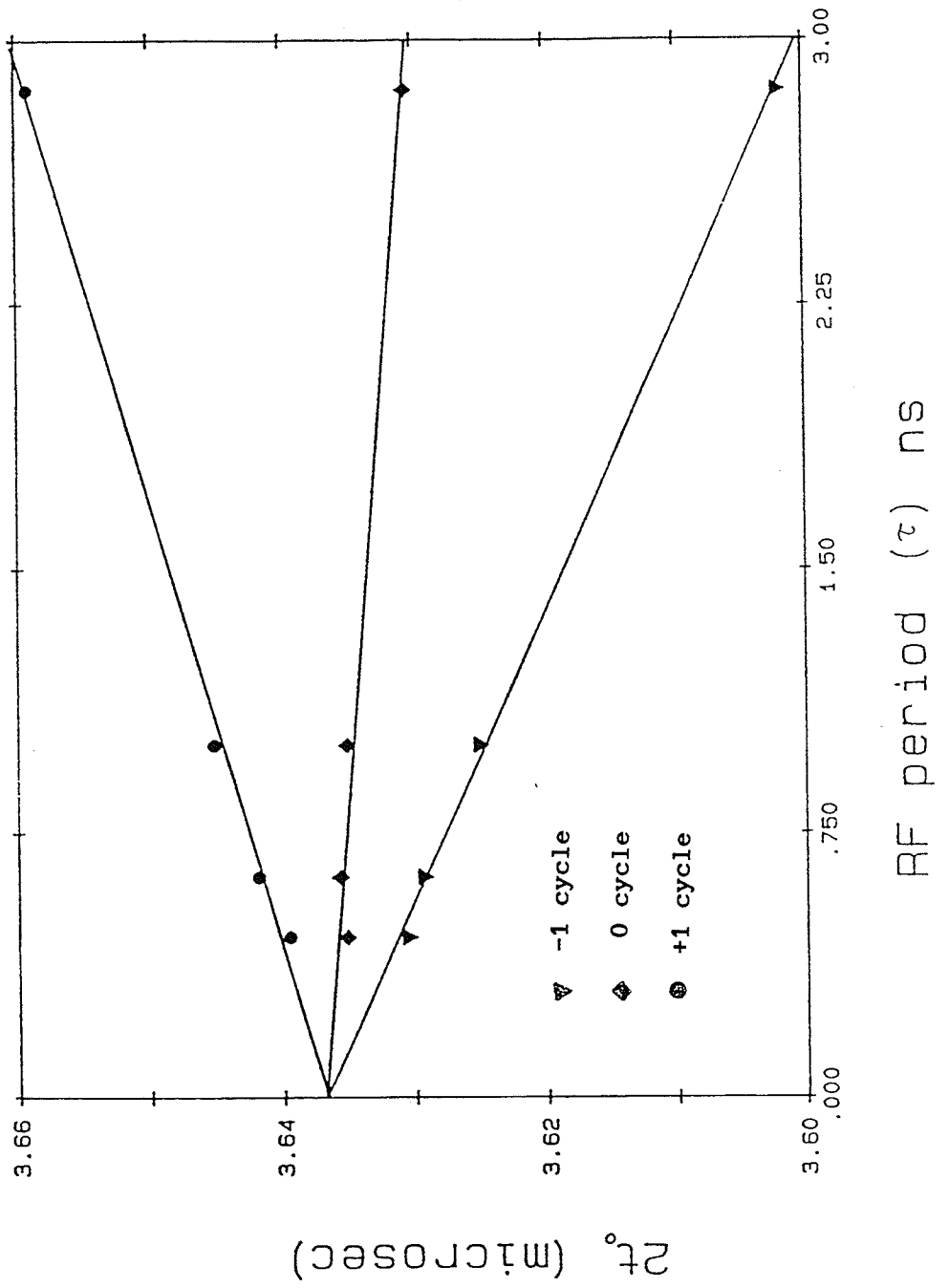


*Figure 3.4 Propagation time between first and second sample echoes in A1 sample, for shear ultrasonic waves.*

## 3.4 SAMPLE POLISHING

In ultrasonic measurements that use the detection of the reflected sample signals by a conventional ultrasonic transducer, it is important to achieve perfect parallelism of the faces of the sample. The faces need to be parallel to a fraction of the wavelength to avoid spurious phase cancellation effects in the piezoelectric transducer.

The sample is mounted in the center of a steel disc using a yellow wax ( #70C Lakeside Brand thermoplastic cement ). The disc thickness depends on the required thickness of the sample ( 0.9mm to 3mm ), and its diameter is about 8cm. The flat faces of the disc are machined parallel to about 10 micrometers. Since the sample is much smaller than the disc diameter, the sample parallelism is better by at least an order of magnitude, enabling the necessary parallelism to be achieved. The crystal axis in which sound is propagated is perpendicular to the flat faces of the sample.

Polishing the sample is then done by first gently *"sanding"* the sample with 500-grit size SiC paper until it is just protruding a fraction of a millimeter from the steel disc. The sample was then polished flush with the steel disc using 6μm diamond paste (Hyprez Diamond compounds) on a stainless steel lap. To achieve a better finish, the sample was then polished on a series of three solder laps, using 6μ,

3μm, and finally 1μm diamond paste. When moving to a finer finish the lap and steel disc were cleaned very carefully using mineral oil which dissolves the diamond paste without damaging the wax, then alcohol, and acetone. This was done to remove all the remaining particles from the previous finish. To test the flatness of the sample, an optical flat slide is placed on the sample and illuminated with a monochromatic light from a Midwest Scientific Company unilamp. If the sample sides are flat the fringes resulting from the light reflected from the optical flat slide and the polished sample face must be parallel lines. Most of the samples are fragile, thus one had to be careful when polishing. Using the above procedure the samples were easily polished to better than 1μm.

## 3.5 SAMPLE BONDING

Bonding was done in two ways, one for the absolute velocity measurements, and the second for the velocity change measurements. The first one, for which the temperature was held constant throughout the measurement, uses silicon oil ( Dow Corning 200 ) as the bonding agent. First the delay rod and sample faces were cleaned carefully using acetone or toluene followed by alcohol. The sample is then bonded using a small drop of silicon oil. The bond needs to be thin enough so that it does not attenuate the sound going to the sample and does not cause an appreciable propagation time error.

The second way of bonding uses a thin ( thickness of 28-45 μm) Indium layer glued to the sample and the delay rod using silicon oil in the same way as above. Indium was used for bonding for the following reasons: a) to provide " *a cushion* " to absorb some of the differences in the thermal expansion and contraction between the sample and the quartz delay rod, and b) to provide a way of looking at a desired region of the sample by cutting the indium piece to the appropriate size (sound will transmit only through the indium piece).

The bonded sample is then placed in a holder under a press of one to two kilograms, and cured over night ( 10 to 12 hours ) at about $65^{0}$C. The bond is then left to cool down for a few hours. This improves the sample signal by up to 10 decibels.

## 3.6 COAXIAL DELAY CABLES CORRECTION

### 3.6.1 INTRODUCTION

For an electromagnetic wave propagating through a cable where losses are present, the attenuation $\alpha$ and the phase velocity v are frequency dependent. For a brief review see, for example, Bleaney and Bleany (1976). Thus it is necessary to correct for the resulting frequency dependent phase shifts in the coaxial cables used to adjust the reference delay in our relative velocity measurements (§ 3.2.1).

For a wave traveling through a cable with capacitance C, inductance L, resistance R, and conductance G per unit length, the phase velocity v and the attenuation $\alpha$ are

$$v=\frac{1}{(LC)^{1/2}}\left\{1-\frac{1}{8\omega^2}\left(\frac{G}{R}-\frac{R}{L}\right)^2\right\},$$

$$\alpha=\frac{1}{2}\left\{R\left(\frac{C}{L}\right)^{1/2}+G\left(\frac{L}{C}\right)^{1/2}\right\}.$$

where the losses represented by R and G are small. Note that the changes in the velocity due to this effect is small ( since it occurs only in second order) and is greatest at low frequencies.

### 3.6.2 METHOD

To measure this effect on our delay data, the apparatus was set as in figure 3.5. A modulated pulse ( obtained as in sections 3.2.1 & 3.2.2) is split into two signals using a power splitter; one signal is used as a reference signal and is passed through a precise attenuator ( 0.0 - 111.0 dB ) to control its level. The other signal is passed through the air filled variable delay lines and the cable being investigated and then its fed into an attenuator ( 0 - 110 dB ). The two signals are then mixed together and viewed on the oscilloscope ( HP1725) which is triggered externally by the Stanford pulse generator.

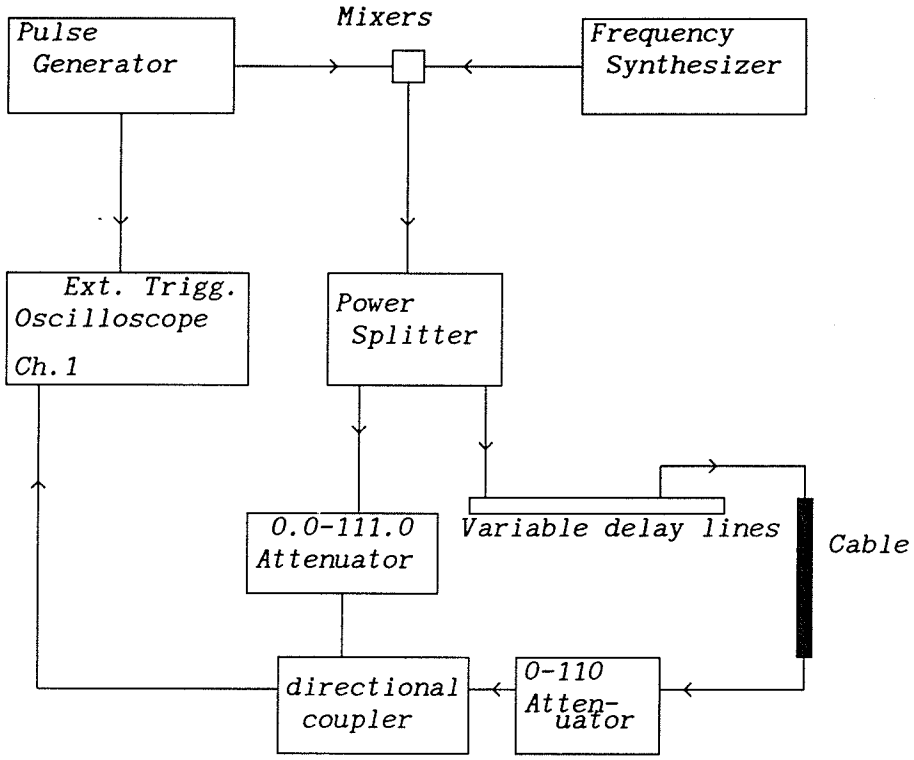


*Figure 3.5 Block diagram for the coaxial cables correction.*

Frequencies of operation $f_n$ were selected using the following condition,

$$f_n = nf_0 = \frac{c}{\lambda} \quad , \text{ and } n = 1 \ , \ 2 \ , \ 3 \ , \ \ldots$$

where $c$ is the speed of light, $\lambda$ is the electrical length of the cable being measured, and $f_0$ is the fundamental frequency corresponding to the cable length. Setting the reference signal level to be the same as the signal passed through the cable under investigation (which can be done to 0.1dB), and varying the delay lines, destructive interference may be achieved and a minimum can be measured to a very good accuracy (2mm). Once a measurement is done the cable is disconnected,and the minimum is measured again. The difference between the two measurements gives the effect on the measured delay (*del*). ( If there were no losses in the cable, the minimum would occur at exactly the same position at all frequencies, and if $f_0$ were chosen exactly as indicated above, the difference between the readings would be zero since adding the cable merely shifts the phase by $2\pi$). The above procedure is repeated for a set of frequencies that are multiples of $f_0$. Results of measurements done on a 1497.6 centimeter cable ( $f_0$= 20 MHz ) are shown in figure 3.6. This method relies on the excellent accuracy of the the frequency synthesizer ( better than one part in $10^7$), to determine the corresponding wavelength $\lambda$ and hence the electrical cable length.

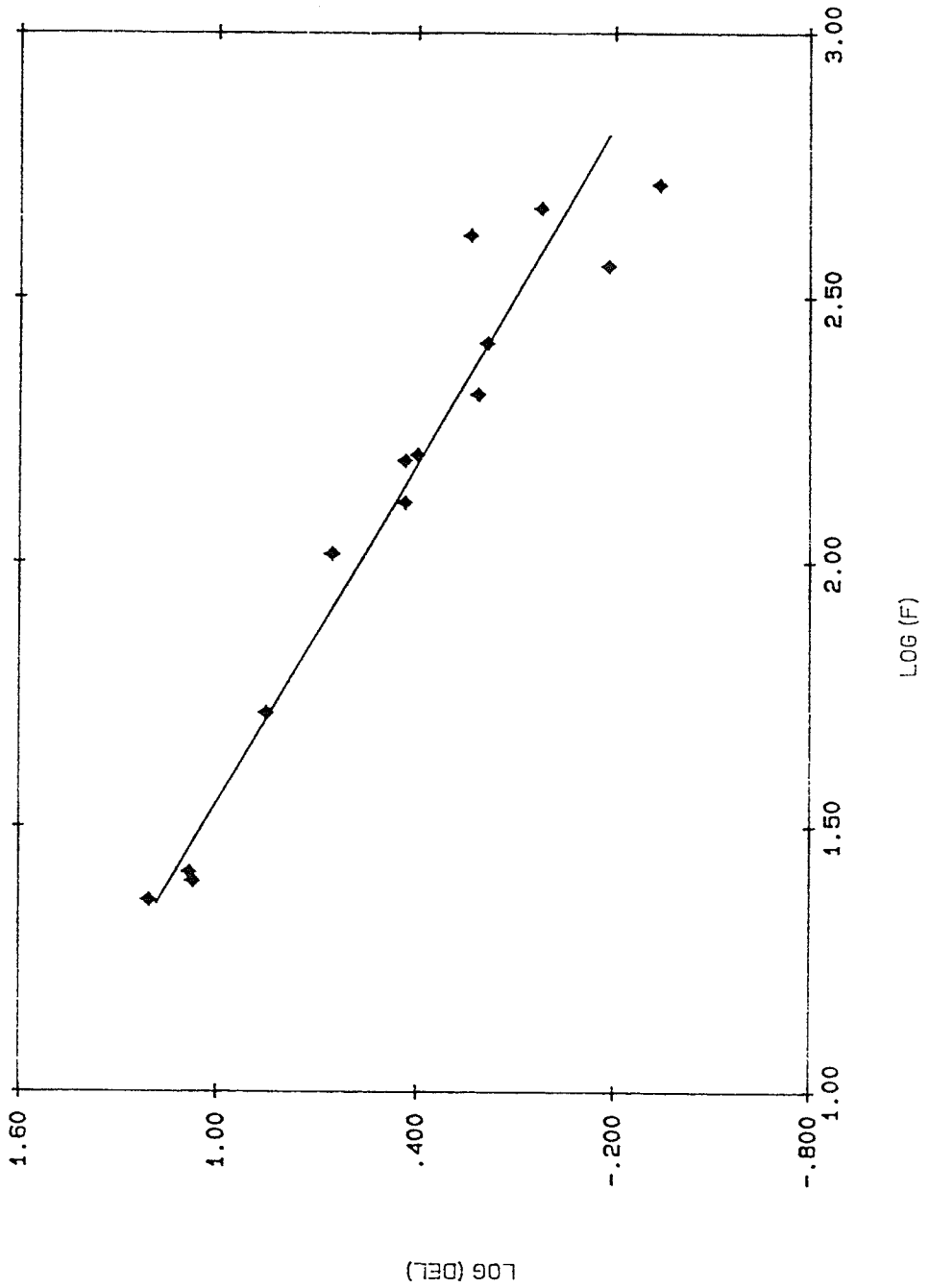


*Figure 3.6 log(del) versus log(F) for 1497.6 cm.*

# CHAPTER FOUR : RESULTS AND DISCUSSION

## 4.1 DATA COLLECTION AND ANALYSIS

In most of our experiments the raw data used to calculate the temperature dependence of the ultrasonic velocity consisted of the delay $D_t$ in centimeters required to cancel the sample echo (see § 3.2.1). The temperature of the sample was measured using a carbon glass resistor whose resistance was easily converted to Kelvin with the use of a calibration curve provided by Lake Shore Cryotronics. A typical result for the total delay $D_t$ as a function of temperature T up to 300K is shown in figure 4.1. These data are for the x=0.15 sample oriented in the [100] direction using longitudinal ultrasonic waves. $D_t$ represents the total delay including the contribution from the quartz delay rod, the indium piece, and the sample. The quartz and indium delays were subtracted from $D_t$ as described in the following section.

### 4.1.1. QUARTZ DELAY ROD CORRECTION

The quartz rod delay was measured separately as a function of temperature the same way as was done for the sample by selecting the reflected quartz echo ($Q_1$ in figure 3.3) and measuring its delay as a function of temperature. To avoid possible spurious shifts, these measurements were performed with the sample removed from the quartz delay rod. The quartz delay was then fitted to a fourth order polynomial

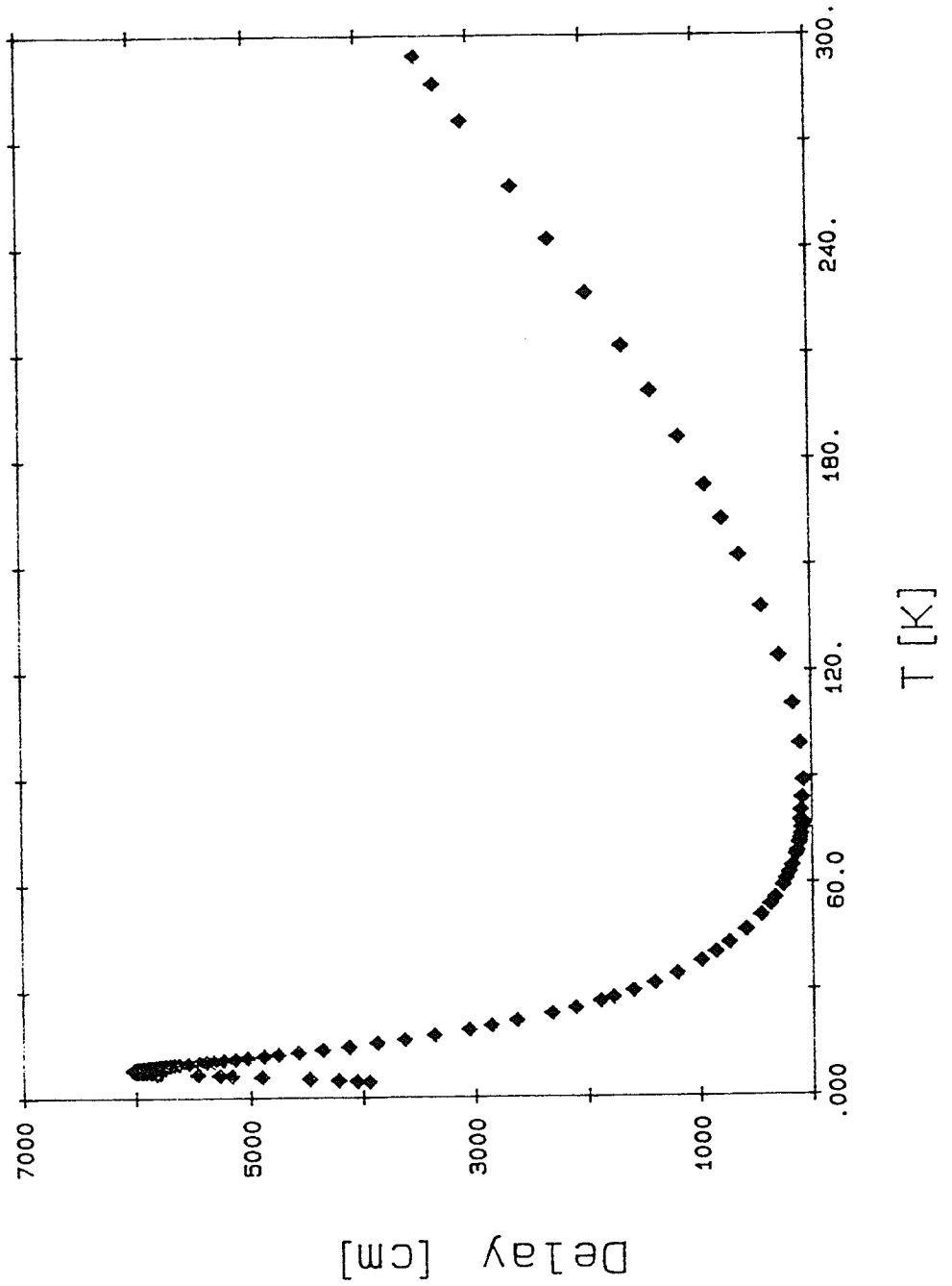


*Figure 4.1 Total delay ( including quartz and indium ) versus temperature for Al sample at 30 MHz.*

and later subtracted from $D_t$. Figure 4.2 shows the polynomial curve used to fit the data with the constant value at zero temperature subtracted. The coefficients of the linear through fourth order terms of this polynomial are respectively: -2.7572, 0.1207, $-3.04\times10^{-4}$, $5.11\times10^{-7}$. The values of the temperature used in this polynomial were obtained from the carbon glass resistor for the data below 77.35 K and the silicon diode thermometer for the data above 77.35 K; to correct for the small temperature discrepancy between the two thermometers at 77.35 K the measured delay was shifted so that the data joined up smoothly at this crossover point.

One of the advantages of using quartz delay rods is that the change in delay is small up to about 20K, so that the shape of the anomaly in the sample velocity is not significantly affected by this correction in the critical region.

### 4.1.2 INDIUM CORRECTION

Appendix I describes how the longitudinal and shear velocities for the indium layer were calculated from the elastic constant data of Chandrasekhar *et al.*(1961). The indium time delay $D_I$ was calculated from

$$D_I=(2s'.\ c)/v,$$

where v is either $v_L$ or $v_S$, $s'$ is the thickness of the indium piece and

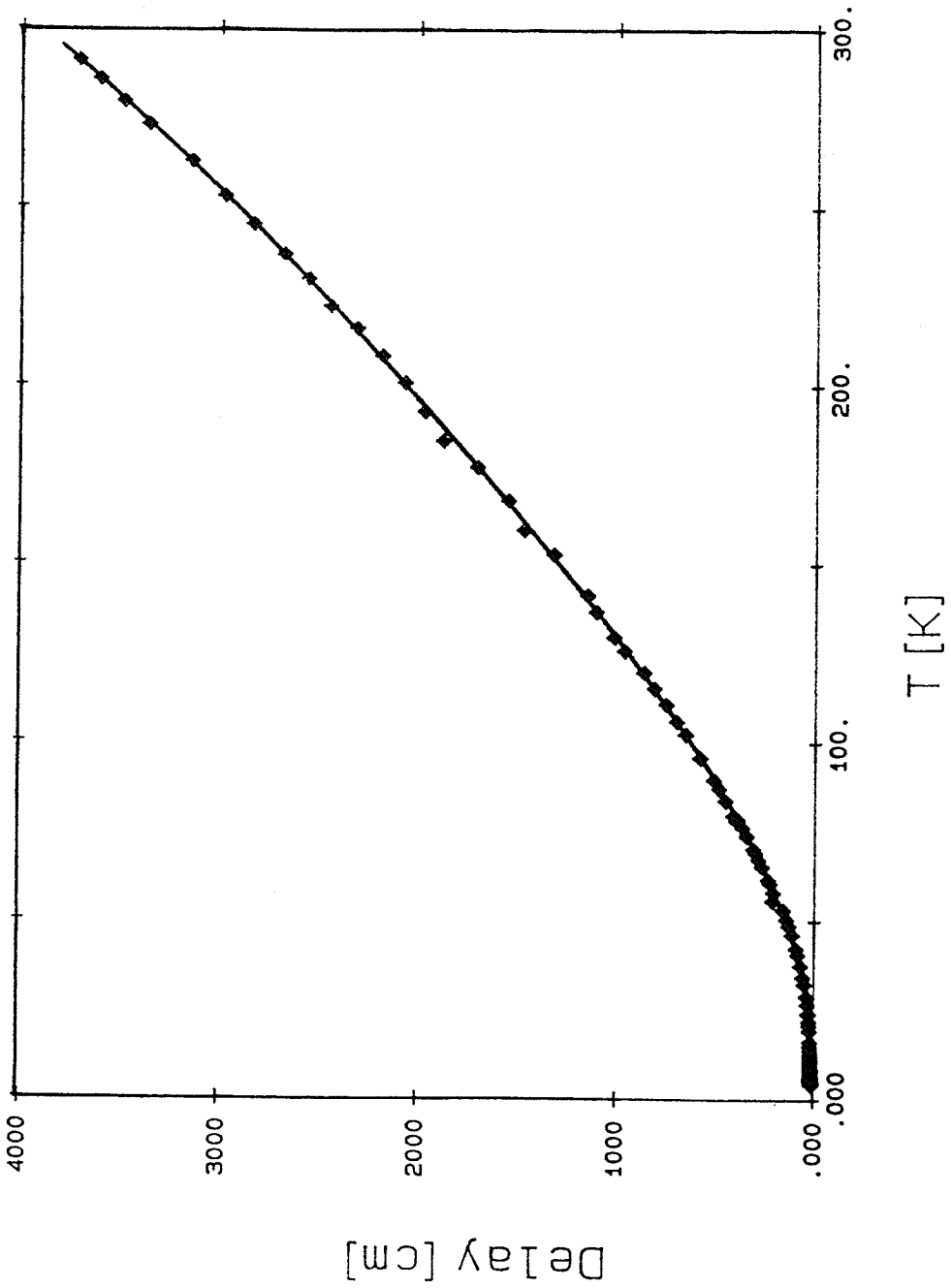


*Figure 4.2 Fifth order polynomial fit to the quartz delay data.*

$c$ is the speed of light. The $D_I$ data were then fit to fourth-order polynomial so that the delay could be subtracted at any temperature T. An example of this correction is given in figure 4.3 for a relatively thick indium piece of thickness 0.147mm. The coefficients of this polynomial are 69.5349, 0.4253, $-1.71\times10^{-4}$, $8.20\times10^{-6}$, and $-1.21\times10^{-8}$. The polynomial is then used for the subtraction. Note that the indium delay variation in the region up to 20K is about 20cm.

### 4.1.3 SAMPLE DELAY

Figure 4.4 shows the *"corrected"* sample delay in which the quartz and indium contributions have been subtracted from the data presented in figure 4.1. Note that the sample delay is almost constant above 90K, and has the largest variation in the region from 8 - 30 K. For this reason the elastic constant and velocity data data will now be presented up to 77 K only.

### 4.1.4 THE ULTRASONIC VELOCITY

The velocity of the ultrasonic pulse in the sample is calculated using the following equation:

$$v = \frac{2\,s}{t_0 + (D-D_0)/c},$$

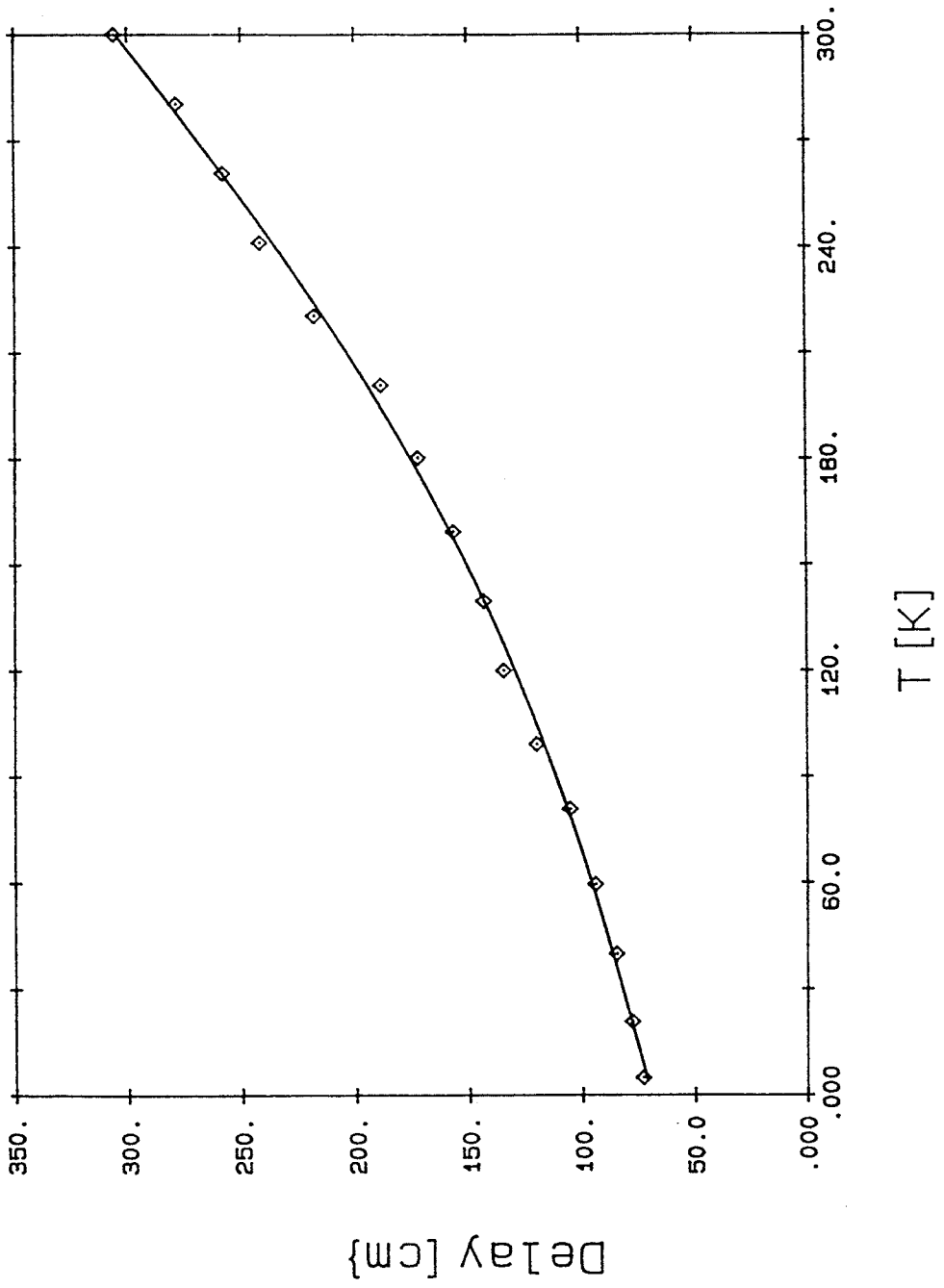


*Figure 4.3 A fourth order polynomial fit to the delay data for an indium layer of thickness 0.147 mm.*

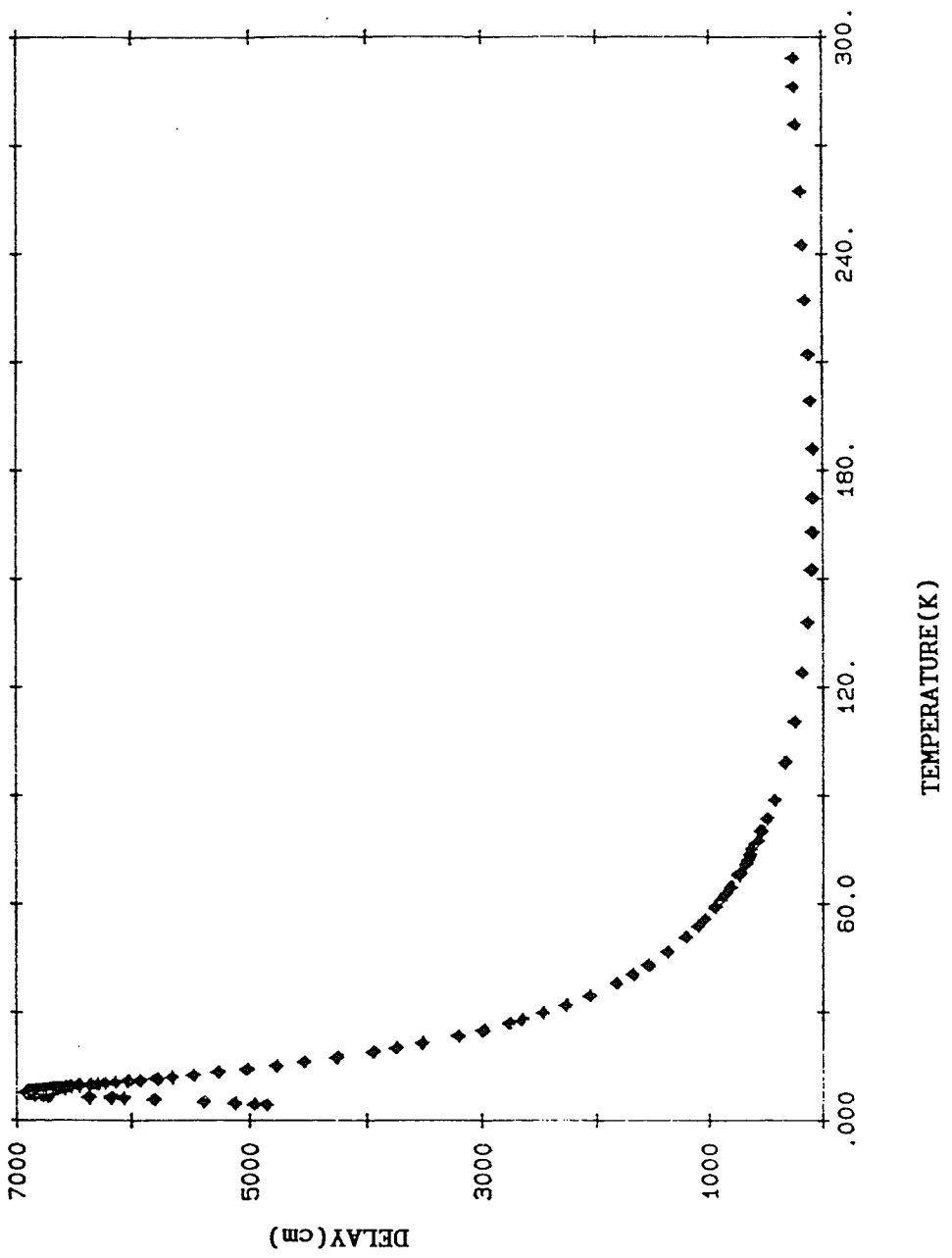


*Figure 4.4 Sample delay ($D_S$-$D_Q$-$D_I$) versus temperature for the [100] sample.*

where $s$ is the sample thickness, $t_0$ is the room temperature propagation time , $D_0$ is the time delay measured at the same temperature as $t_0$, and $D$ is the measured variable delay. An example of velocity data at 30MHz, calculated from the delay plotted in figure 4.4, is shown in figure 4.5. It shows that the velocity of [100] longitudinal waves slows down dramatically as the phase transition temperature is approached.

## 4.2 DETERMINATION OF THE ELASTIC CONSTANTS

Table 4.1 shows the elastic constants that were measured using elastic waves propagating in a tetragonal crystal oriented along [100] and [110] crystal axes. For a review of the determination of the different elastic constants from sound velocity measurements see Neighbours *et al.* (1967). The table shows that the soft mode elastic constant $\frac{1}{2}(c_{11}-c_{12})$ can be measured directly using transverse waves propagating along [110] direction. However, previous experiments (Melcher, *et al.*(1972) and Graham, *et al.*(1991)) have shown that the ultrasonic attenuation for this mode is too high for measurements to be performed in the critical region close to $T_D$. To avoid this difficulty $\frac{1}{2}(c_{11}-c_{12})$ was measured indirectly from $c_{11}$ using the velocity v of the longitudinal ultrasonic waves propagating along the [100] direction for which $c_{11}=\rho v^2$, where $\rho$ is the the sample density. This method relies on the fact that $c_{11}$ can be written as the sum of two symmetrized elastic constants

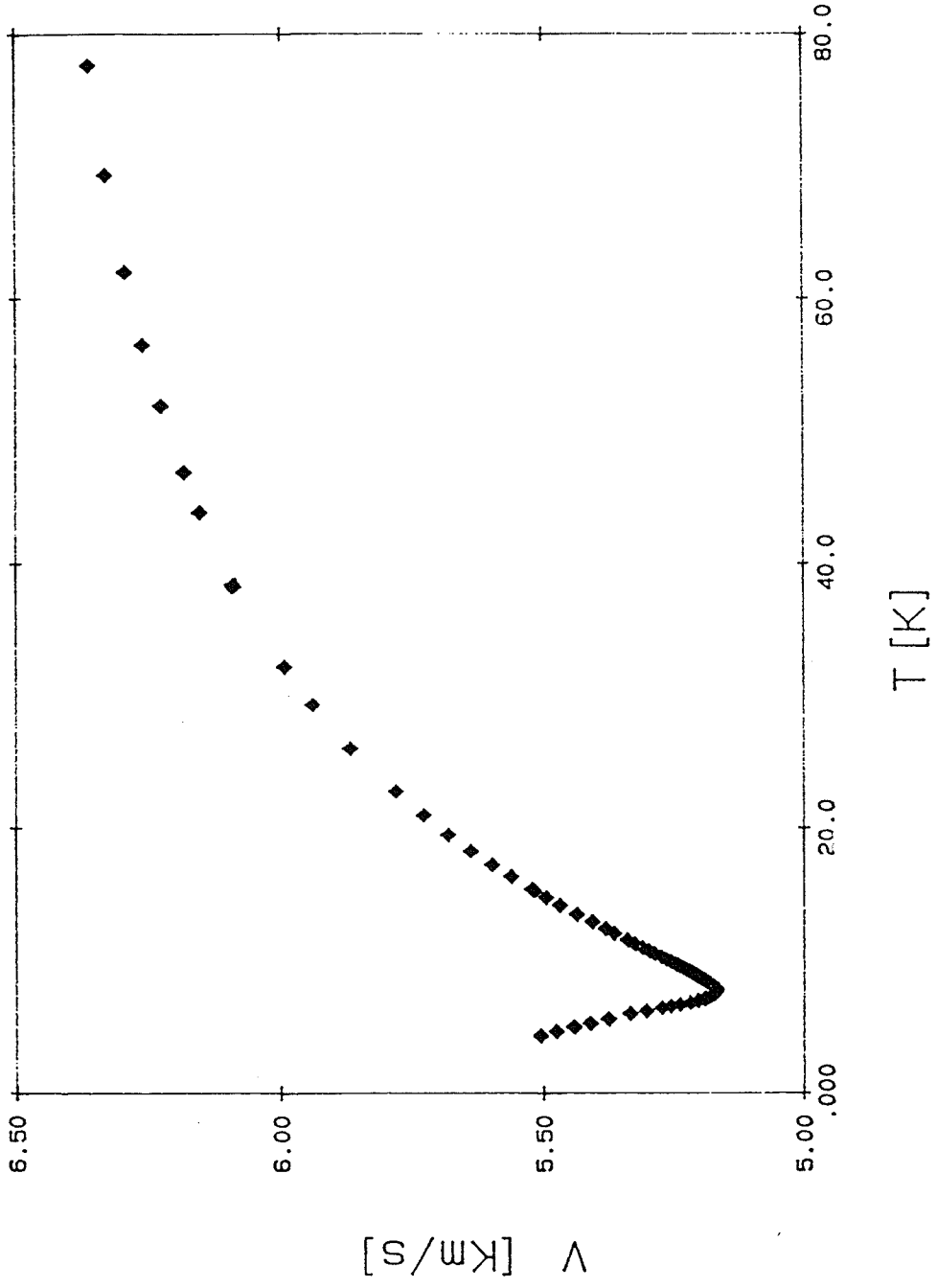


*Figure 4.5 Longitudinal ultrasonic velocity versus temperature for [100] sample at 30 MHz.*

**TABLE (4.1)**

Elastic constants for ultrasonic waves with propagation and polarization directions in the basal plane of a tetragonal crystal. Here **k** is the ultrasonic wave vector as, **u** is the displacement, $\rho$ is the density of the sample, and **v** is the velocity.

| *polarization direction* **k** | *ultrasonic waves* | *elastic constant*= $\rho v^2$ |
|---|---|---|
| [100] | longitudinal **u** ∥ [100] | $c_{11}$ |
| [100] | transverse **u** ∥ [010] | $c_{66}$ |
| [110] | longitudinal **u** ∥ [110] | $1/2(c_{11}+c_{12})+c_{66}$ |
| [110] | Transverse **u** ∥ [1$\bar{1}$0] | $1/2(c_{11}- c_{12})$ |

$$c_{11} = \frac{1}{2}(c_{11}+c_{12}) + \frac{1}{2}(c_{11}-c_{12}) \qquad (4.1)$$

Since the elastic constant $\frac{1}{2}(c_{11}+c_{12})$ corresponds to an $A_{1g}$ strain which has the wrong symmetry to couple to the distortion, it is expected to remain constant through the transition ( see § 4.4 below), enabling the temperature dependence of $\frac{1}{2}(c_{11}-c_{12})$ to be determined from $c_{11}$.

The results of $c_{11}$ measurements on three [100] samples as function of temperature are shown in figure 4.6 and table 4.2. The values of the densities used to calculate the elastic constants were computed from room temperature X-ray measurements of the lattice constants as described in Taylor *et al.*(1990). The three elastic constant curves decrease continuously to a minimum value at the transition temperature $T_D$ due to the softening of $\frac{1}{2}(c_{11}-c_{12})$. The lack of any discontinuity in $\frac{1}{2}(c_{11}-c_{12})$ at $T_D$ indicates that the phase transition is second order, as in pure $DyVO_4$, and not first order, as in $DyAsO_4$. Table 4.2 shows that the transition temperature is lowered as the arsenic concentration x is increased, which indicates that the random field strains are stronger for the higher concentrations. The reduction in $T_D$ with respect to pure $DyVO_4$ ($T_D$=14.6K) is considerable in these samples, indicating that strong random fields are generated. Note that the transition temperatures for the two samples from the same batch *B* (*B1* and *B2*) are not identical, suggesting either that the concentrations x

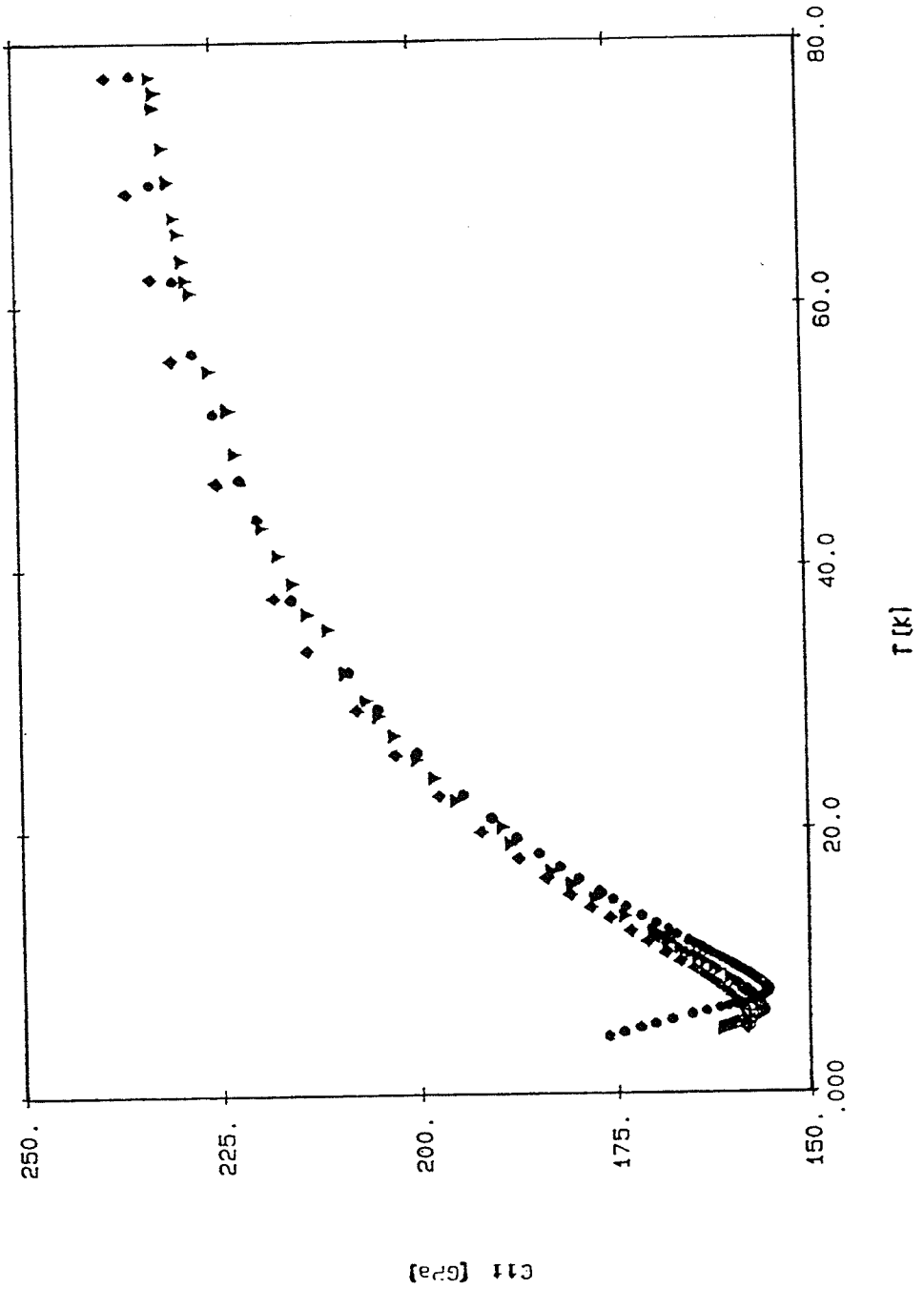


*Figure 4.6 Elastic constant $c_{11}$ versus temperature for all [100] samples ( ● A1, ▲ B1 and ◆ B2 ).*

**TABLE 4.2**

Summary of the data for $c_{11}$ measurements in the three [100]samples. $x$ is the arsenic concentration of each sample, $s$ is the thickness of the sample, $T_D$ is the transition temperature, and $c_{11}(T_D)$ is the elastic constant at the transition temperature $T_D$.

| *sample rientation* | $x$ | *s(mm)* | $T_D$(K) | $c_{11}(T_D)$ GPa | $T_D/(T_D)_{pure}$ |
|---|---|---|---|---|---|
| [100] | 0.154 | 2.926∓0.002 | 7.77±0.02 | 155.35±0.02 | 0.53 |
| [100] | 0.164 | 0.917∓0.002 | 6.24±0.03 | 156.33±0.02 | 0.42 |
| [100] | 0.164 | 2.916∓0.002 | 5.43±0.01 | 157.87±0.02 | 0.37 |

in the two samples are not the same or that different amounts of flux impurities in the two samples are introducing additional random strains which are larger in sample *B2*. Since concentration gradients within a sample have been found to be very small (Taylor *et al.*1990), it is difficult to see how two samples from the same batch could have sufficiently different values of x to explain the different transition temperatures. The other possibility, that flux impurities are responsible, is difficult to verify quantitatively, although both samples were selected from the batch because of their optical clarity which is generally associated with a low flux concentration. Another feature of the data shown in figure 4.6 is that the minimum becomes broader as the concentration x is increased. One possible contribution to the rounding of the phase transition could be the effect of inhomogeneities which cause the distortion temperature to be different in the different regions of the sample. This effect was investigated using a birefringence technique by Graham and co-workers (Graham (1990) and Taylor *et al.* (1990)) for two of our samples (*A1* and *B2*). They found that concentration inhomogeneities, even in the worst sample studied (*A1*), were too small to significantly affect the observed broadening of the transition.

Another possible contribution to the rounding of the transition is dynamic non-equilibrium effects due to the extreme slowing down of the critical fluctuations as the transition is approached. Although there

have been several theoretical predictions (Villain (1985), Fisher (1986)), the only experimental evidence in random-field systems is that of Jaccarino *et al* (1988), and Nash *et al.*(1991), who used AC susceptibility measurements on the dilute antiferromagnet $Fe_{0.46}Zn_{0.54}F_2$ to study dynamic rounding over a wide range of frequencies. They found that random fields in their system cause a measurable rounding of the transition at frequencies as low as 5mHz and were able to show that the dynamical critical behavior of $Fe_{0.46}Zn_{0.54}F_2$ is better described by an activated dynamics model as first suggested by Villain and Fisher. In the next section we examine this effect in our RF system $Dy_xAsV_{1-x}O_4$ for the three samples *A1*, *B1*, and *B2* having concentrations x= 0.154, 0.164, 0.164 respectively.

## 4.3 DYNAMIC CRITICAL BEHAVIOR

To investigate the dynamic effects, the elastic constant $c_{11}$ was measured for the three [100] samples: *A1* with x = 0.154, $s$ = 2.926 mm and in the range 11 MHz to 70 MHz, *B1* with x = 0.164, $s$ =.917 mm and in the range 25 MHz to 120 MHz, and *B2* with x = 0.164, $s$ =2.916 mm and in the range 25 MHz to 70 MHz. The upper limit of the frequency range for each sample was determined by the ultrasonic attenuation, which increased quadratically with frequency in the region down to the transition temperature and which became so large near $T_D$ at high frequencies that the sample echoes were too small to measure. The

results of these measurements are shown in figures 4.7, 4.8, and 4.9.

From these results the following observations can be made:

A) Both samples *B1* in the range 25 MHz to 120 MHz, and *B2* in the range 25 MHz to 70 MHz show that the minimum $c_{11}$ value and the corresponding temperature $T_{min}$ increase as the frequency increases. This indicates that for these two samples, in which the random fields are strong (x=0.164), dynamic effects are present and contribute to the rounding of the phase transition; in other words the elastic constant for these random field systems (*B1* and *B2* ) depends on the frequency in the critical region.

B) For the *A1* sample (x=0.154), in which the random fields are weaker, the elastic constant is independent of frequency, and no dynamic rounding is observed. This implies that no dynamic rounding of the phase transition occurs in the range from 11 MHz to 70 MHz.

For each sample the temperature dependence of the elastic constant was the same at all frequencies for temperatures between the upper edge of the critical region and 15-20 K, although there were small frequency-dependant discrepancies at higher temperatures. A possible explanation of this spurious effect is discussed below. The data shown in figures 4.7, 4.8, and 4.9 were corrected for such discrepancies by overlaying the data in the temperature range 8-12 K where the slopes dc/dT were the same.

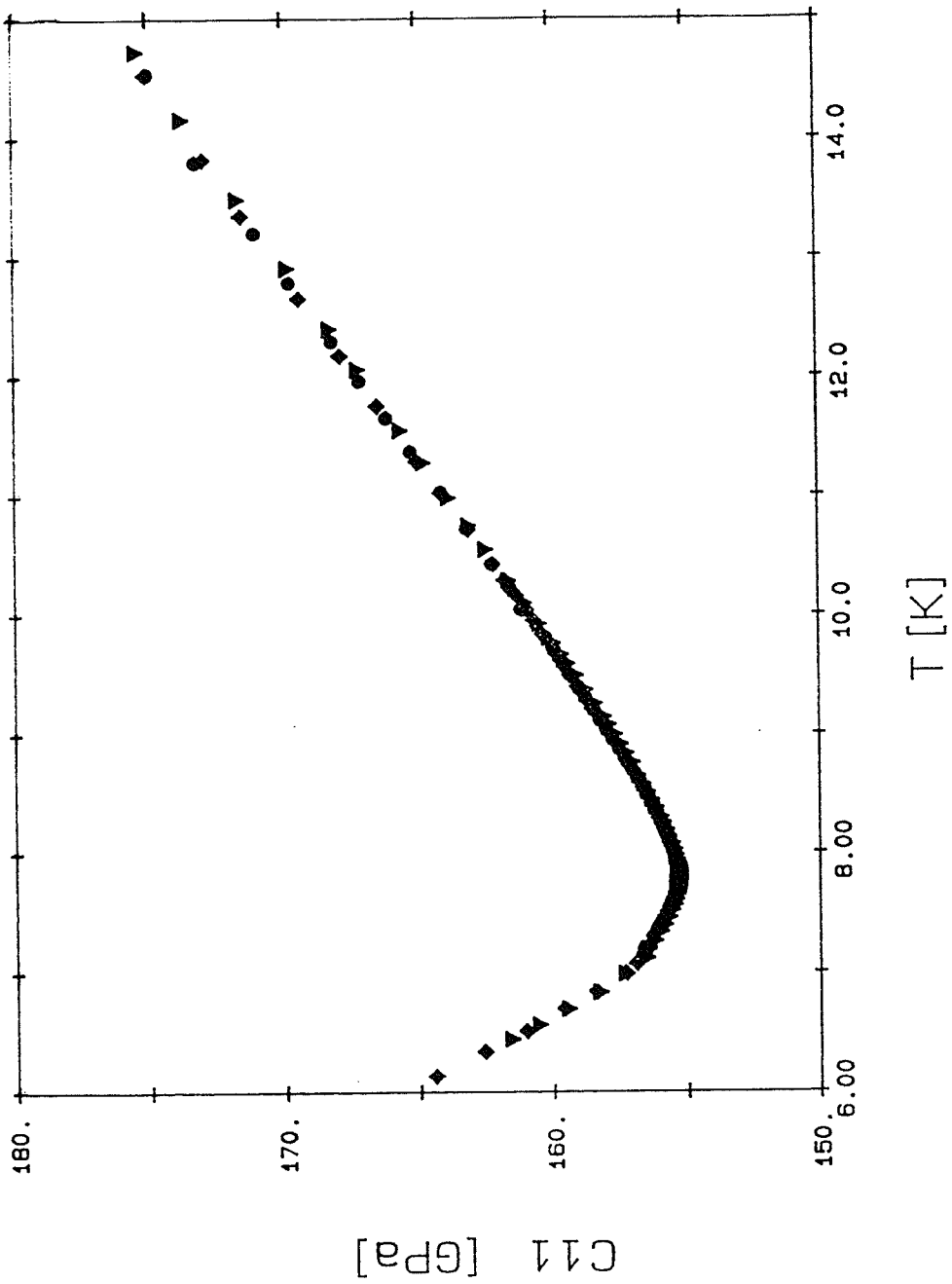


*Figure 4.7* **a)** *The elastic constant* $c_{11}$ *versus temperature for sample A1 at ▲ 30 MHz, ◆ 50 MHz and ● 70 MHz.*

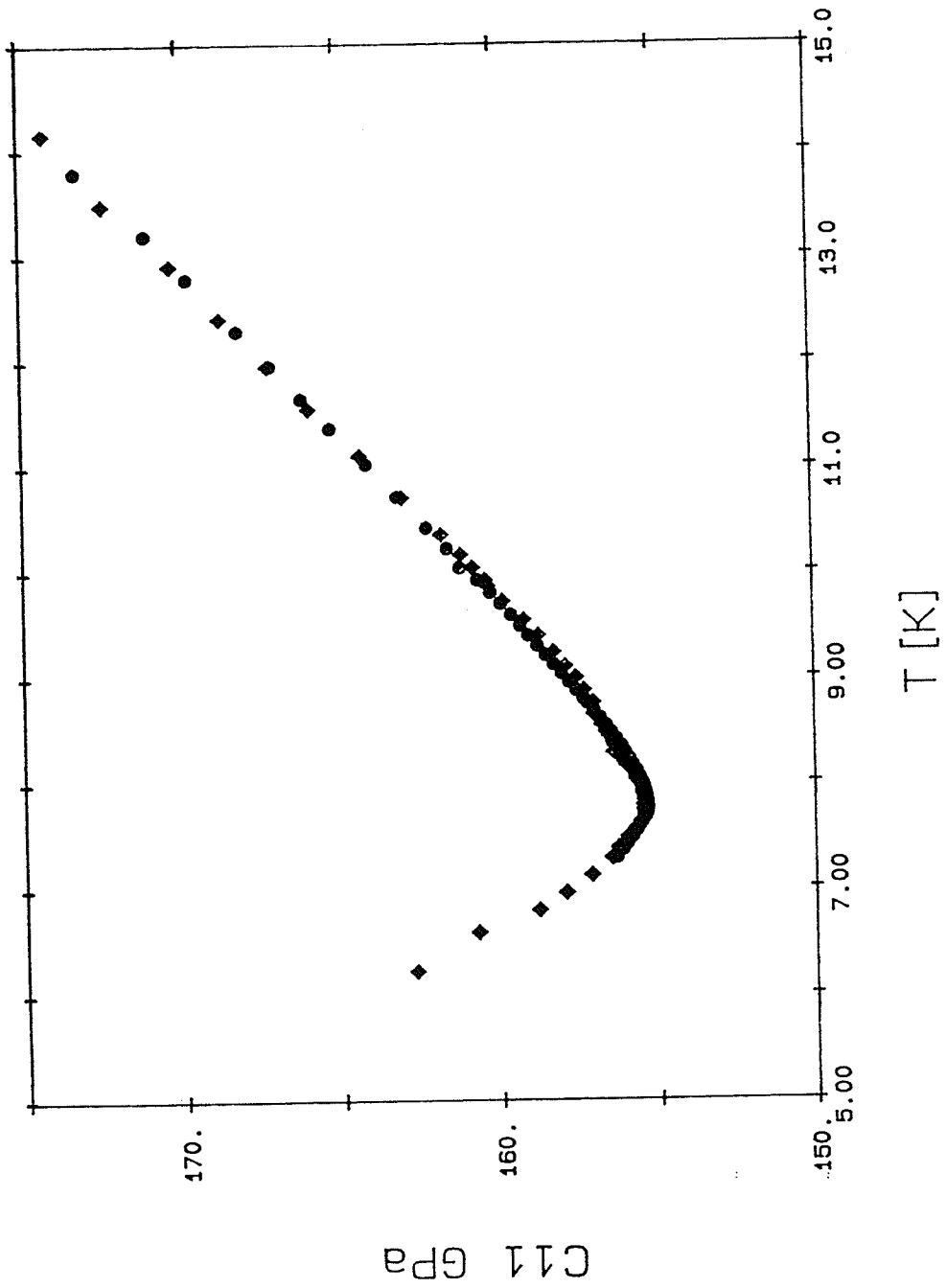


*Figure 4.7* **b)** *Elastic constant* $c_{11}$ *versus temperature for sample A1 at* ■ *11 MHz and* ● *70 MHz.*

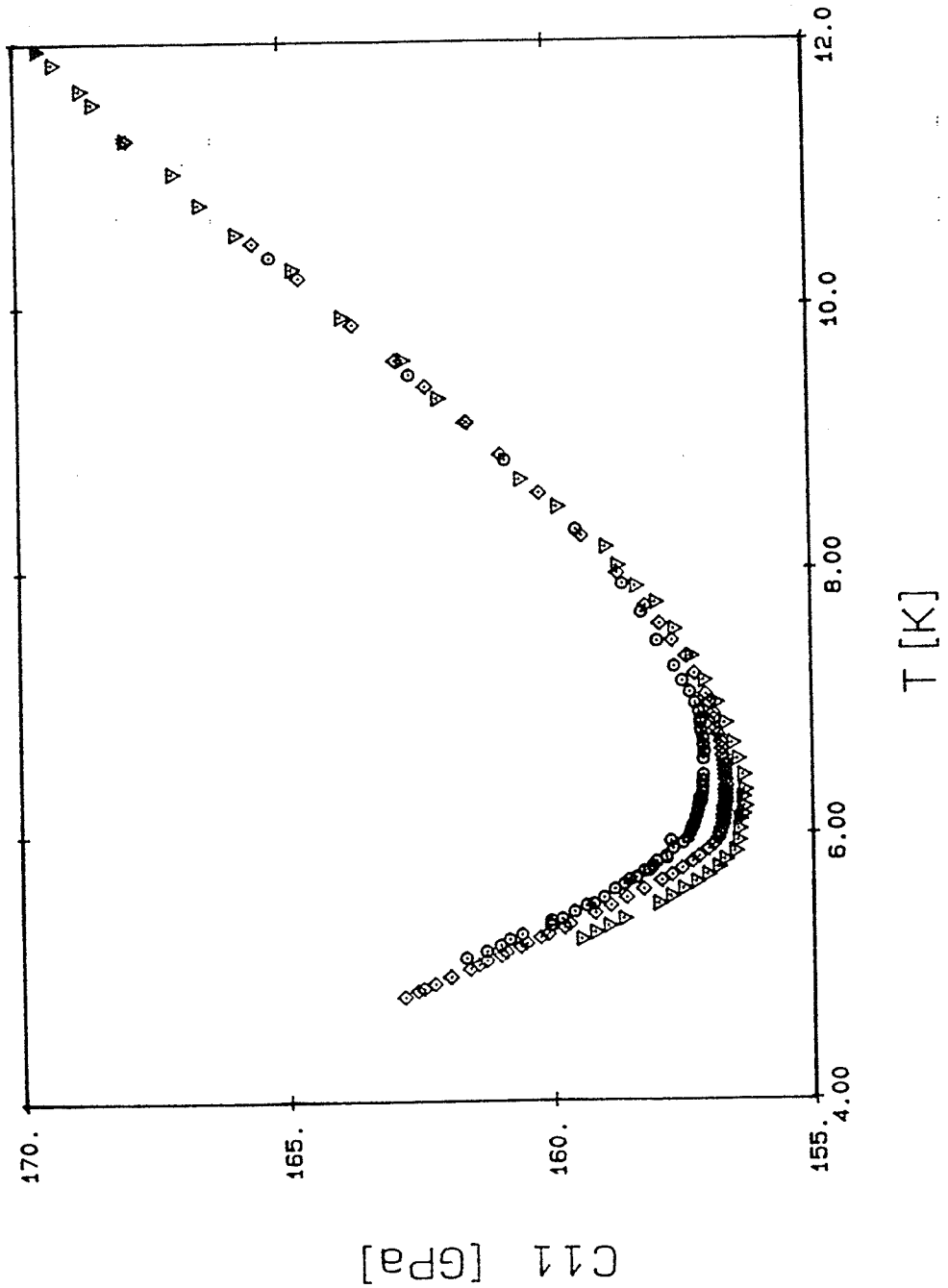


*Figure 4.8 Elastic constant $c_{11}$ versus temperature for sample B1 at* △ *25 MHz,* ◇ *68 MHz and* ⊙ *120 MHz.*

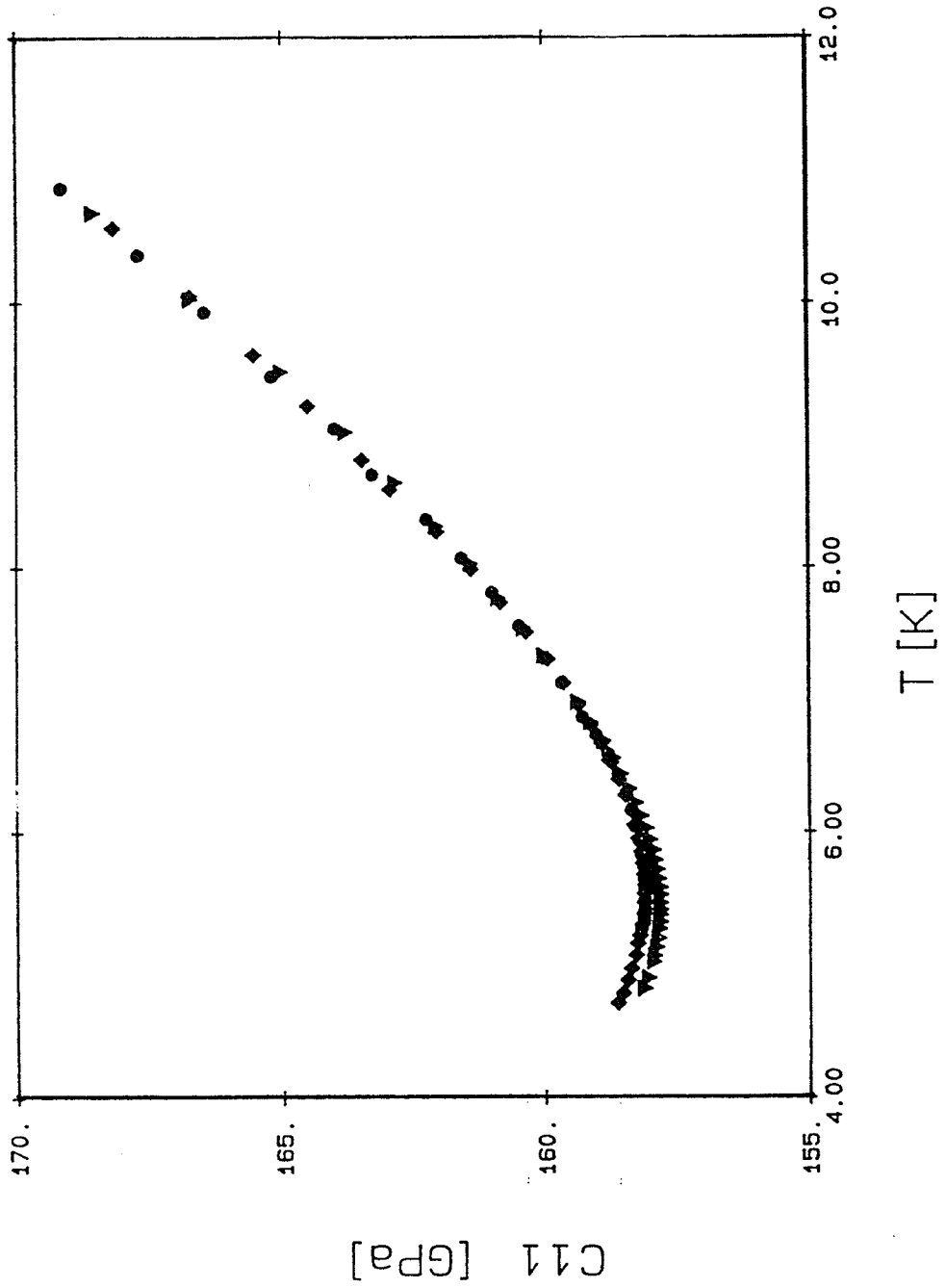


*Figure 4.9* **a)** *Elastic constant* $c_{11}$ *versus temperature for sample B2 at* ▲ *30 MHz,* ◆ *50 MHz and* ● *70 MHz.*

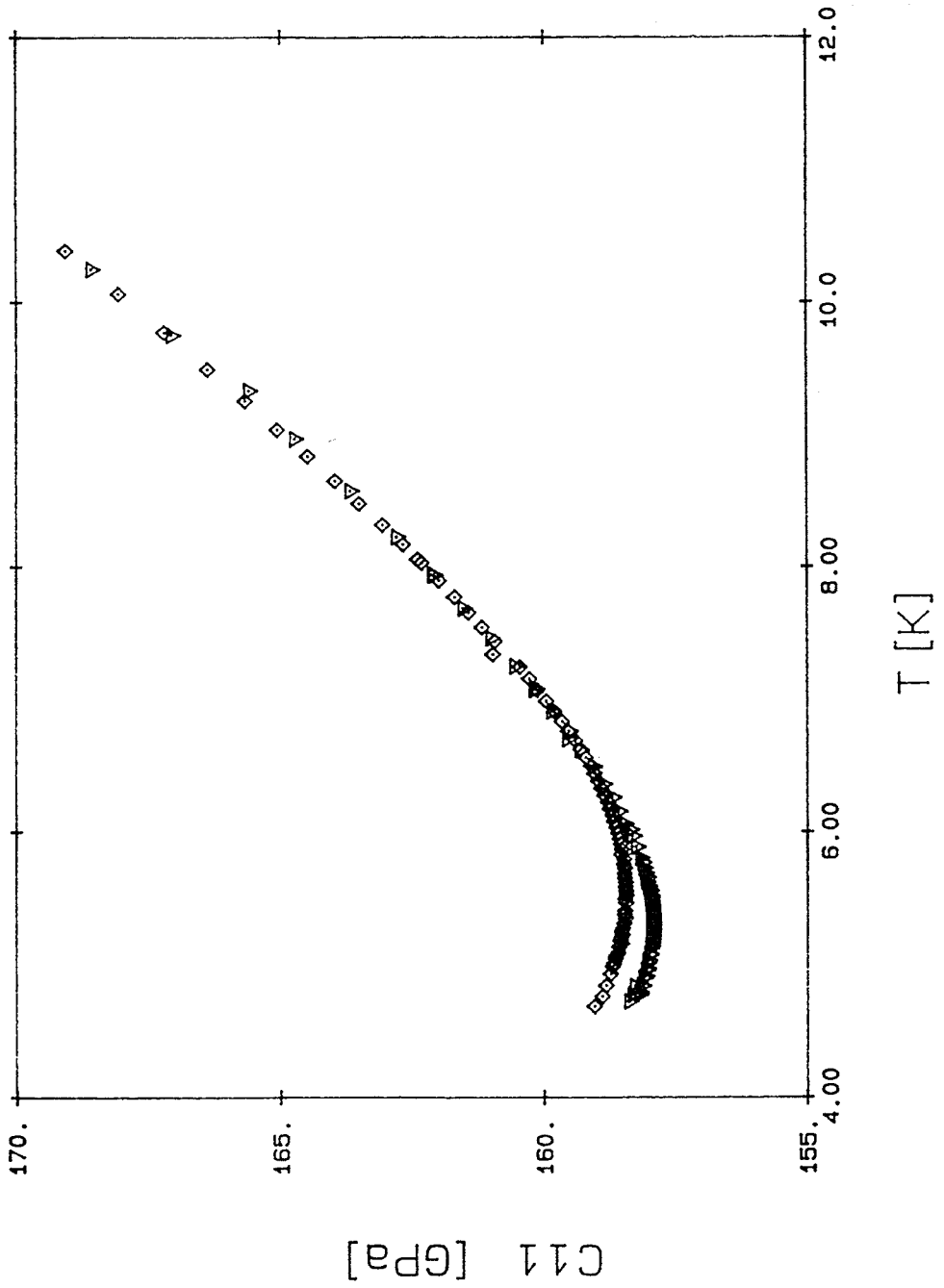


*Figure 4.9* **b)** *Elastic constant for sample B2 at* △ *25 MHz and* ◇ *68 MHz.* (Note that the data here is not corrected for indium).

Before discussing the implications of the dynamic rounding observed in samples *B1*, *B2*, it is important to establish that there were no significant contributions from spurious frequency-dependent effects such as interference with background signals or multiple reflections with the indium layer. Interference with the background signals ( see § 3.2.2) could introduce a measurable phase shift in the sample echo, leading to errors in the delay measurements that vary with the ultrasonic frequency. This problem was most serious near the phase transition temperature for high frequency measurements where the attenuation of the ultrasonic pulse was greatest and the continuous background pick-up largest. To calculate the the phase shift due to this background signal, we write the measured signal as a linear combination of the background signal and the sample signal,

$$A_M \sin(\omega t+\phi_M) = A_S \sin(\omega t+\phi_S)+A_B \sin(\omega t+\phi_B),$$

Here A and $\phi$ represent the signal amplitude and phase respectively, and the subscripts M, S, and B stand for measured, sample, and background respectively. This expression can be inverted to solve for the phase shift $\phi_S-\phi_M$, giving

$$(\phi_S-\phi_M)=\sin^{-1}(A_B/A_S \sin(\phi_M-\phi_B)).$$

The maximum phase shift is

$$(\phi_S-\phi_M)_{max} = \sin^{-1}(A_B/A_S)$$

Thus the maximum error in the delay $\delta$ is

$$\delta=\{\lambda/2\pi\}(\phi_S-\phi_M).$$

The amplitudes of the sample and background signals used to calculate $\phi_S-\phi_M$ were estimated from the measured attenuation data for each sample and the size of the background at the position of the sample echo. (The background signals were measured after the runs were completed and the sample removed from the delay rod, so that the background could be separated from the sample signal). The results for these calculations are summarized in table 4.3 for samples *B1* and *B2* in which the dynamic effects were observed. Since a delay error of 1cm corresponds to an error in the elastic constant of 0.01 GPa for sample *B2* and 0.03 GPa for sample *B1*, it is clear that interference with the background is too small to account for the observed frequency dependence, and that it is generally comparable to the scatter of the data due to finite resolution of the spectrometer.

A second possible source of spurious phase shifts is interference due to multiple reflections in the indium layer. The attenuation of the indium layer is lowest at low frequencies, and hence the interference effect due to the indium layer would be greatest at low frequencies. For a 30 μm indium piece the transit time t ≃ 20nsec and the corresponding delay is *c*t = 600cm, where *c* is the speed of light. This could generate

**TABLE 4.3**

Results of calculations of the maximum delay error introduced by interference with the background signals. *a*) sample *B1*, and *b*) sample *B2*, Here F is the frequency, T is the temperature, and $\delta$ is the maximum delay error.

**(a)**

| F[MHz] | T [K] | *Estimated Ratio* $A_S/A_B$ | $\delta$ (cm) |
|---|---|---|---|
| 25 | 77 | 178 | 1.07 |
| | $T_D$ | 172 | 1.11 |
| 68 | 77 | 223 | 0.38 |
| | $T_D$ | 100 | 0.70 |
| 120 | 77 | 3.2 | 4.30 |
| | $T_D$ | 5.6 | 7.00 |

**(b)**

| F[MHz] | T[K] | *Estimated ratio* $A_S/A_B$ | $\delta$ (cm) |
|---|---|---|---|
| 30 | 77 | 32 | 5.00 |
| | $T_D$ | 22 | 7.20 |
| 50 | 77 | 100 | 0.95 |
| | $T_D$ | 40 | 2.40 |
| 70 | 77 | 36 | 1.20 |
| | $T_D$ | 8.9 | 7.70 |

huge phase shifts on both the signals entering and leaving the sample. Writing the measured signal amplitude as follows,

$$A_M \sin(\phi_M - \phi_S) = A_S + A_1 \sin\phi_I + A_2 \sin 2\phi_I + \ldots,$$

where $\phi_I$ is the phase shift introduced by a single round trip in the indium layer and each term accounts for the contribution due to successive round trips. In the region where the longitudinal indium velocity is not changing ( the temperature region up to about 20 K see figure I.1 ) $\phi_I$ remains constant, and the amplitudes $A_1$, $A_2$,... should not change significantly relative to $A_S$, so that the change in delay with temperature in this region is not affected by such shifts. Hence the change in the elastic constant near the phase transition is independent of interference effects involving the indium layer. However, this effect could introduce a measurable phase shift at higher temperatures, and is probably the cause of the small frequency dependent discrepancies observed in the change in the elastic constant between 20 K and 70 K noted above.

These calculations clearly indicate that the dynamic effects shown in figures 4.8 and figure 4.9 cannot be explained by spurious interference effects. We therefore conclude that the dynamic rounding observed in samples *B1* and *B2* is a genuine dynamic critical effect resulting from the extreme slowing down of the critical fluctuations as

the transition temperature is approached. The fact that these dynamic effects are observed in the two samples with the strongest random fields but not in the sample having weaker random fields strongly suggests that the critical slowing down is greatly enhanced by random fields, as predicted by Villain and Fisher. Qualitatively our data for samples *B1* and *B2* agree with dynamic scaling predictions that the minimum in the elastic constant $c_{min}(\omega)$, the corresponding temperature $T_{min}(\omega)$ and the temperature $T^{*}_{min}(\omega)$ at which non-equilibrium effects set in all increase with frequency, albeit weakly. Figure 4.10 and figure 4.11 show the frequency dependence of $c_{min}(\omega)$ and $T_{min}(\omega)$ over the limited frequency range that could be achieved in the present experiments. The corresponding data are also summarized in table 4.4. However the frequency range of the data is too limited to make a quantitative comparison with the Fisher's dynamic scaling model (see § 2.5.2), especially as the logarithmic dependence on the frequency is so weak. The difficulty in making a meaningful comparison between theory and experiment is compounded by the number of unknowns in equations 2.5.1 and 2.5.2 for $t_{min}(\omega)$ and $c_{min}(\omega)$: data close to the static limit are needed to pin down $T_D$ and $c_{min}(\omega=0)$ before the characteristic frequency $\omega_o$ and the product of the exponents $\nu$ and $\theta$ can be reasonably determined from the elastic constant data. Finally it should also be pointed out that data over a much wider frequency range are needed to unambiguously show whether or not our structural random-field system is indeed correctly described by Fisher's activated dynamics model or whether it

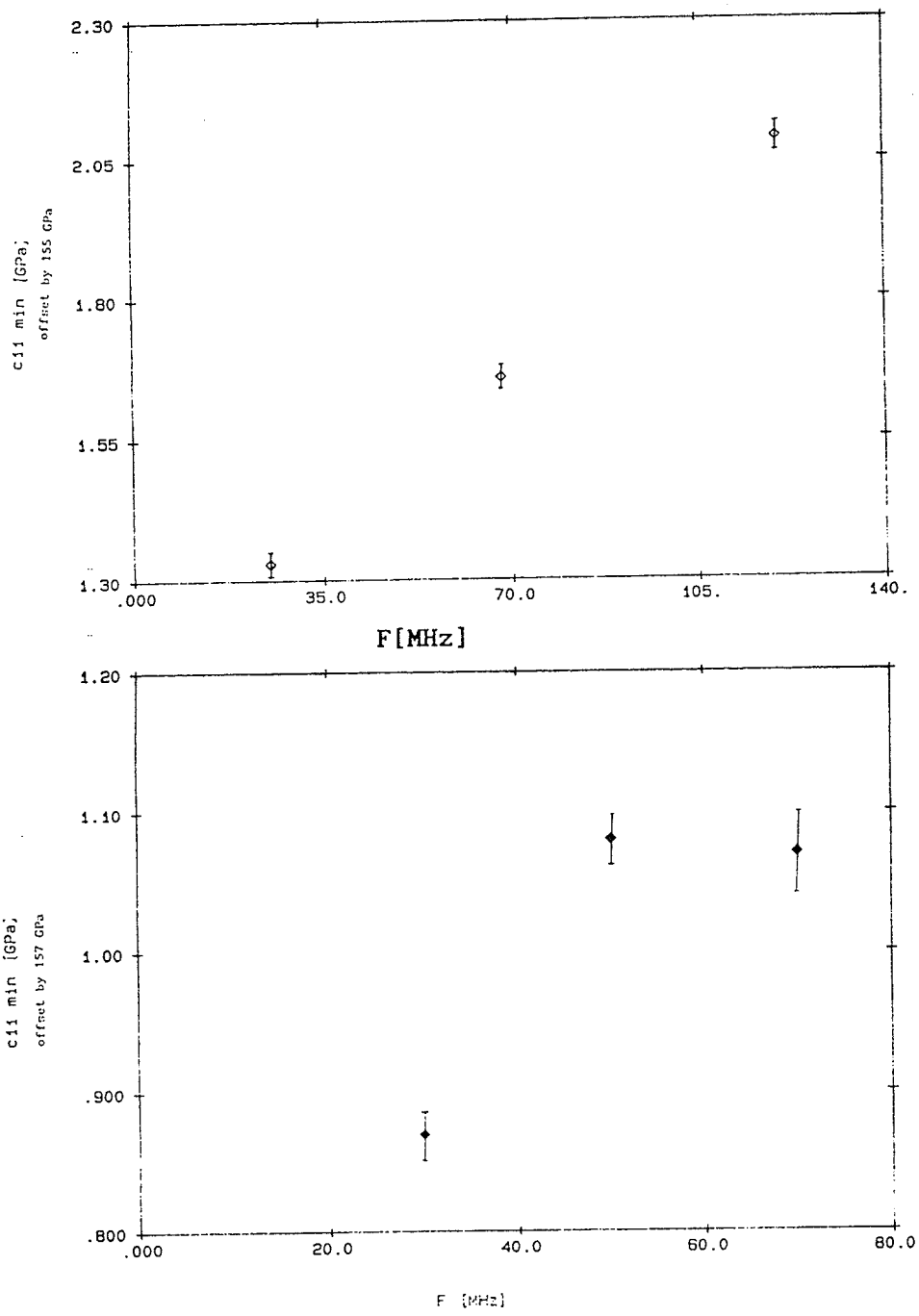


*Figure 4.10 Elastic constant* $c_{min}(\omega)$ *versus frequency:* **a)** *sample B1* **b)** *sample B2.*

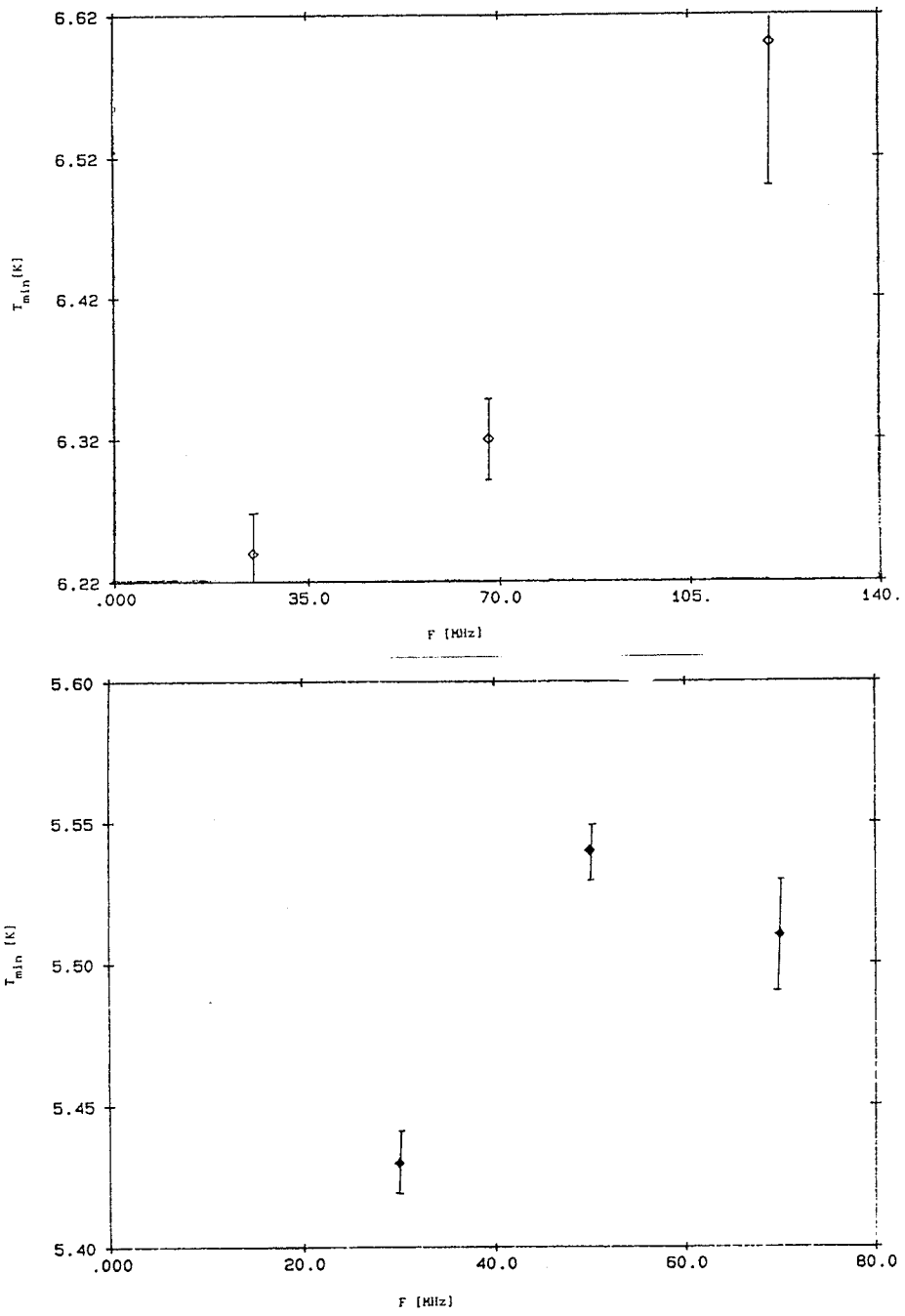


*Figure 4.11 Temperature* $T_{min}(\omega)$ *versus frequency:* **a)** *sample B1*

**b)** *sample B2.*

**TABLE 4.4**

The results of the $c_{11}$ measurements for the three [100] samples: *A1, x=0.15, and s=2.926mm, B1; x=0.17, and s=0.917, B2; x=0.17, and s=2.915.*

| *Sample* | *frequency* [MHz] | $T_{min}$ [K] | $c_{min}$ [GPa] |
|---|---|---|---|
| *A1* | 11 | 7.78±0.02 | 155.35±0.05 |
| | 30 | 7.77±0.02 | 155.35±0.02 |
| | 50 | 7.77±0.02 | 155.34±0.01 |
| | 70 | 7.77±0.02 | 155.35±0.01 |
| *B1* | 25 | 6.24±0.03 | 156.33±0.02 |
| | 68 | 6.32±0.03 | 156.66±0.02 |
| | 120 | 6.60±0.1 | 157.09±0.03 |
| *B2* | ‡ 25 | 5.29±0.02 | 157.97±0.02 |
| | 30 | 5.43±0.01 | 157.87±0.02 |
| | 50 | 5.54±0.01 | 158.08±0.02 |
| | ‡ 68 | 5.52±0.02 | 158.44±0.02 |
| | 70 | 5.51±0.02 | 158.07±0.03 |

‡ These data are calculated with no indium correction.

whether it is better described by *"conventional"* dynamic scaling in which the characteristic time $\tau$ has a power-law dependence on the correlation length ( $\tau \propto \xi^{z}$ ).

## 4.4 STATIC CRITICAL BEHAVIOR

For sample *A1*, the elastic constant $c_{11}$ was found in the previous section (figures 4.9 and 4.10) to be independent of frequency in the range 10MHz to 70MHz, implying that the static critical behavior of the soft mode elastic constant $\frac{1}{2}(c_{11}-c_{12})$ is not obscured by the dynamics in these measurements. To investigate the static critical behavior, the temperature dependence of the soft mode elastic constant $\frac{1}{2}(c_{11}-c_{12})$ was determined in the critical region as follows ( see equation 4.2.1 and table 4.1):

1) $c_{11}$ was measured from the [100] longitudinal ultrasonic velocity (Figure 4.5).

2) $\frac{1}{2}(c_{11}+c_{12})+c_{66}$ was measured from the [110] longitudinal ultrasonic velocity of a second sample cut from the same crystal. These data are shown in figure 4.12.

3) $c_{66}$ was measured from the velocity of transverse ultrasonic waves propagating along the [100] direction and polarized in the basal plane as shown in figure 4.13.

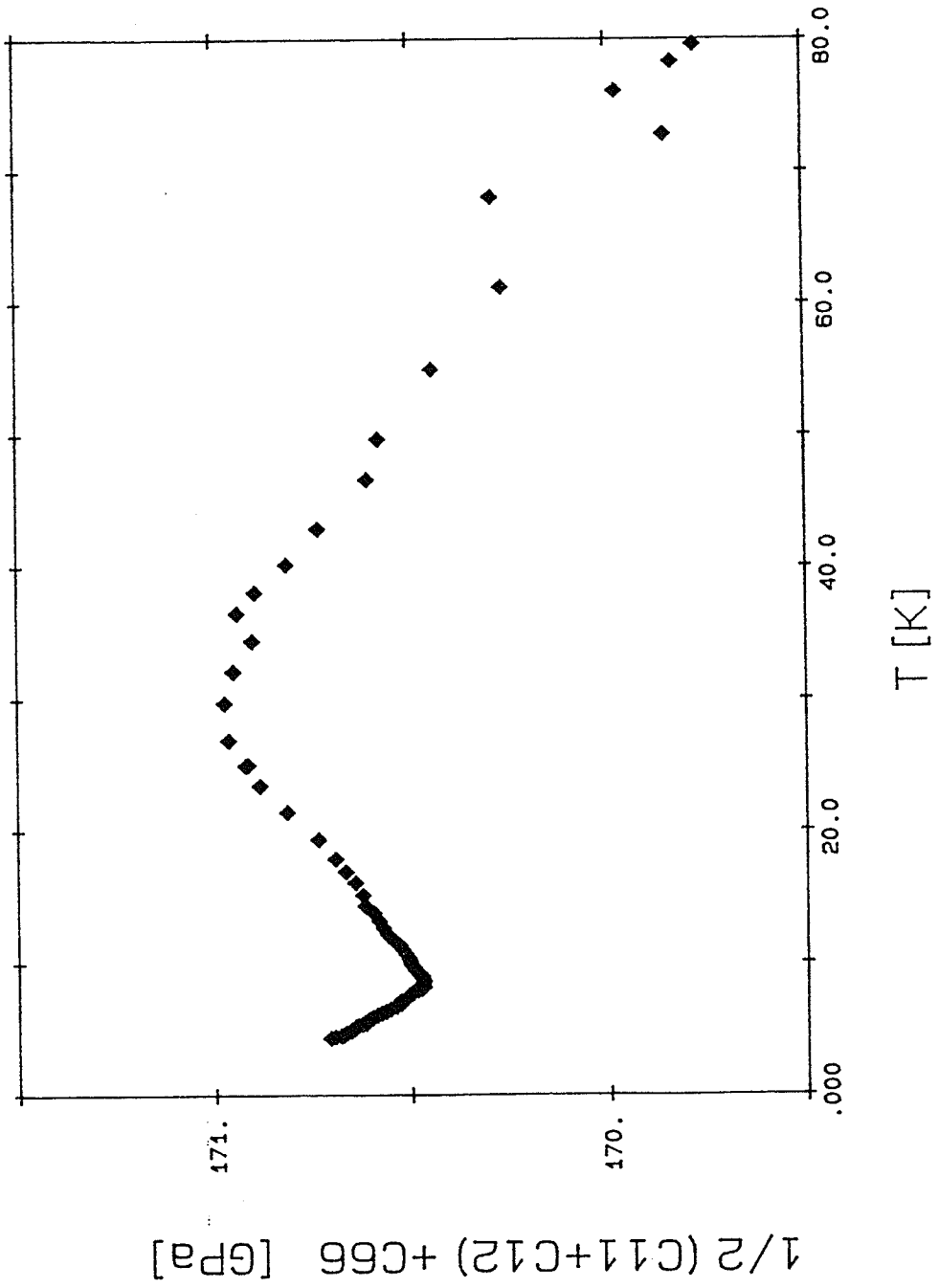


*Figure 4.12 Elastic constant* $1/2(c_{11}+c_{12})+c_{66}$ *versus temperature {corrected for the misaligment}*

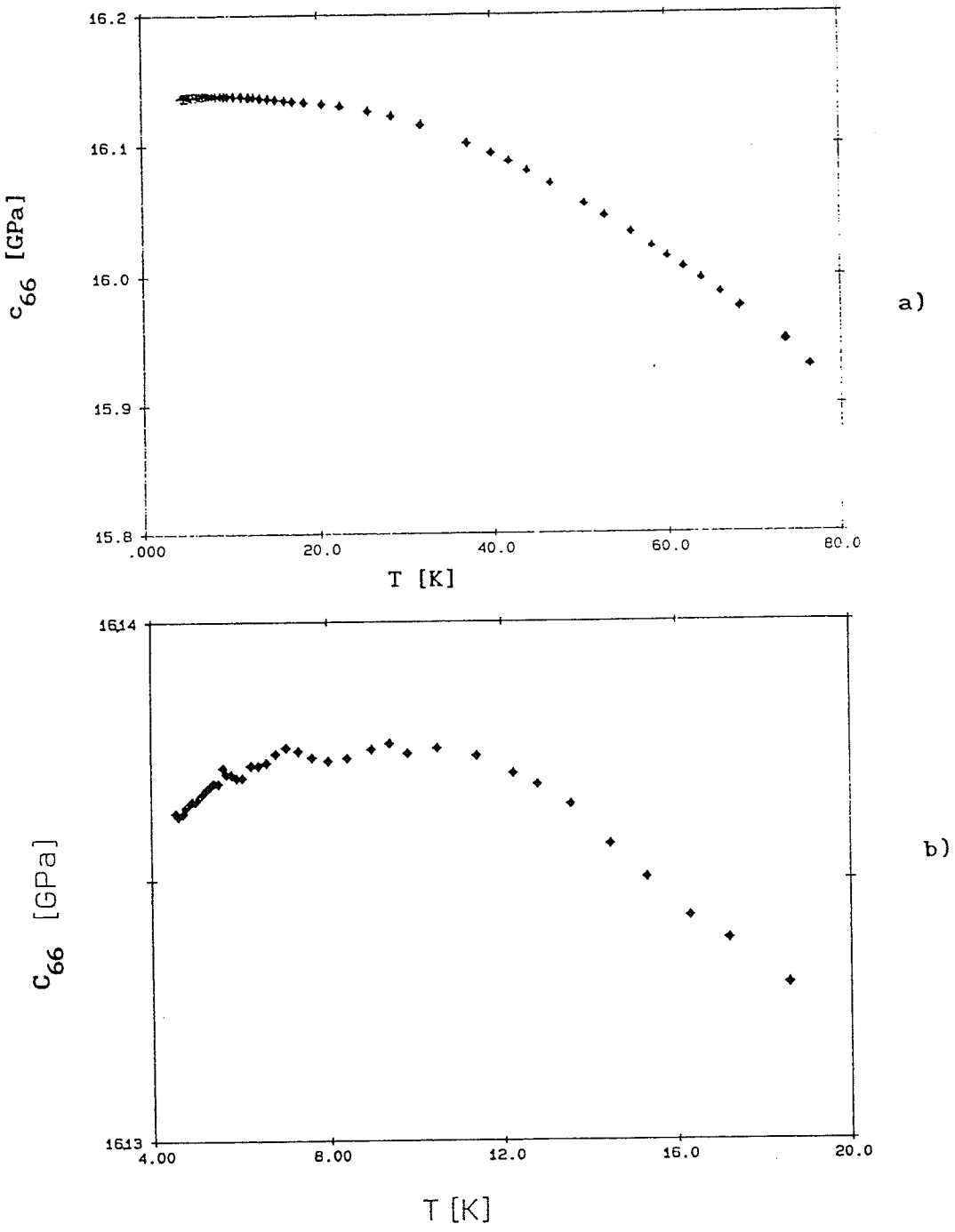


*Figure 4.13 Elastic constant* $c_{66}$ *versus temperature.* **a)** *up to 80* K **b)** *up to 20* K.

4) $\frac{1}{2}(c_{11}+c_{12})$ was calculated by subtracting a fourth order polynomial curve fitted to the $c_{66}$ data from $\frac{1}{2}(c_{11}+c_{12})+c_{66}$. The result is shown in figure 4.14.

5) $\frac{1}{2}(c_{11}-c_{12})$ was then calculated by fitting a seventh order polynomial to $\frac{1}{2}(c_{11}-c_{12})$ and subtracting this curve from the data for $c_{11}$ shown in figure 4.4. See Figure 4.15.

The data for $\frac{1}{2}(c_{11}+c_{12})+c_{66}$ (figure 4.12) show a small anomaly near $T_D$ which is similar in shape to the much larger variation in $c_{11}$. Above about 30K, the elastic constant softens somewhat due to anharmonic effects, a feature characteristic of all elastic constant data which is of no future interest here. By contrast, the data for $c_{66}$ in figure 4.13 shows almost no variation up to 20K. In particular there is almost no indication of any softening of this elastic constant as the transition is approached, indicating that a linear Jahn-Teller coupling to this $B_{2g}$ mode, while allowed by symmetry, is extremely weak. ( In fact these data show that the $B_{2g}$ coupling in this sample is even weaker than expected on the basis of calculations done by Elliott *et al.* (1972) for pure $DyVO_4$). Close examination of figure 4.13b suggests that, instead of decreasing near $T_D$, $c_{66}$ shows a very slight increase, possibly due to higher order coupling to the electronic levels. In any case the variation of $c_{66}$ near the phase transition is far too small to account for any of the observed anomaly in $\frac{1}{2}(c_{11}+c_{12})+c_{66}$.

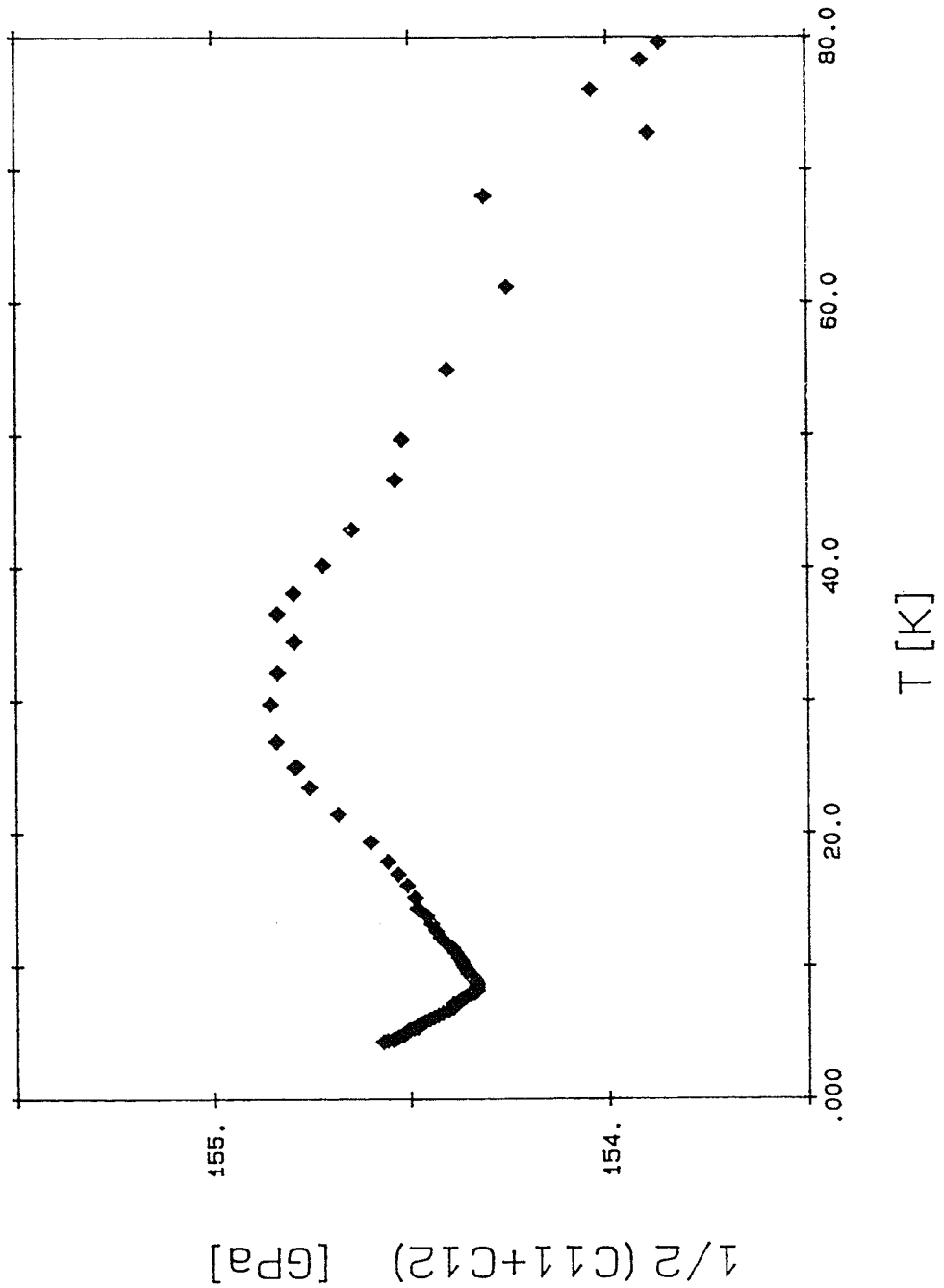


*Figure 4.14 Elastic constant* $1/2(c_{11}+c_{12})$ *calculated by subtracting* $c_{66}$ *from* $1/2(c_{11}+c_{12})+c_{66}$.

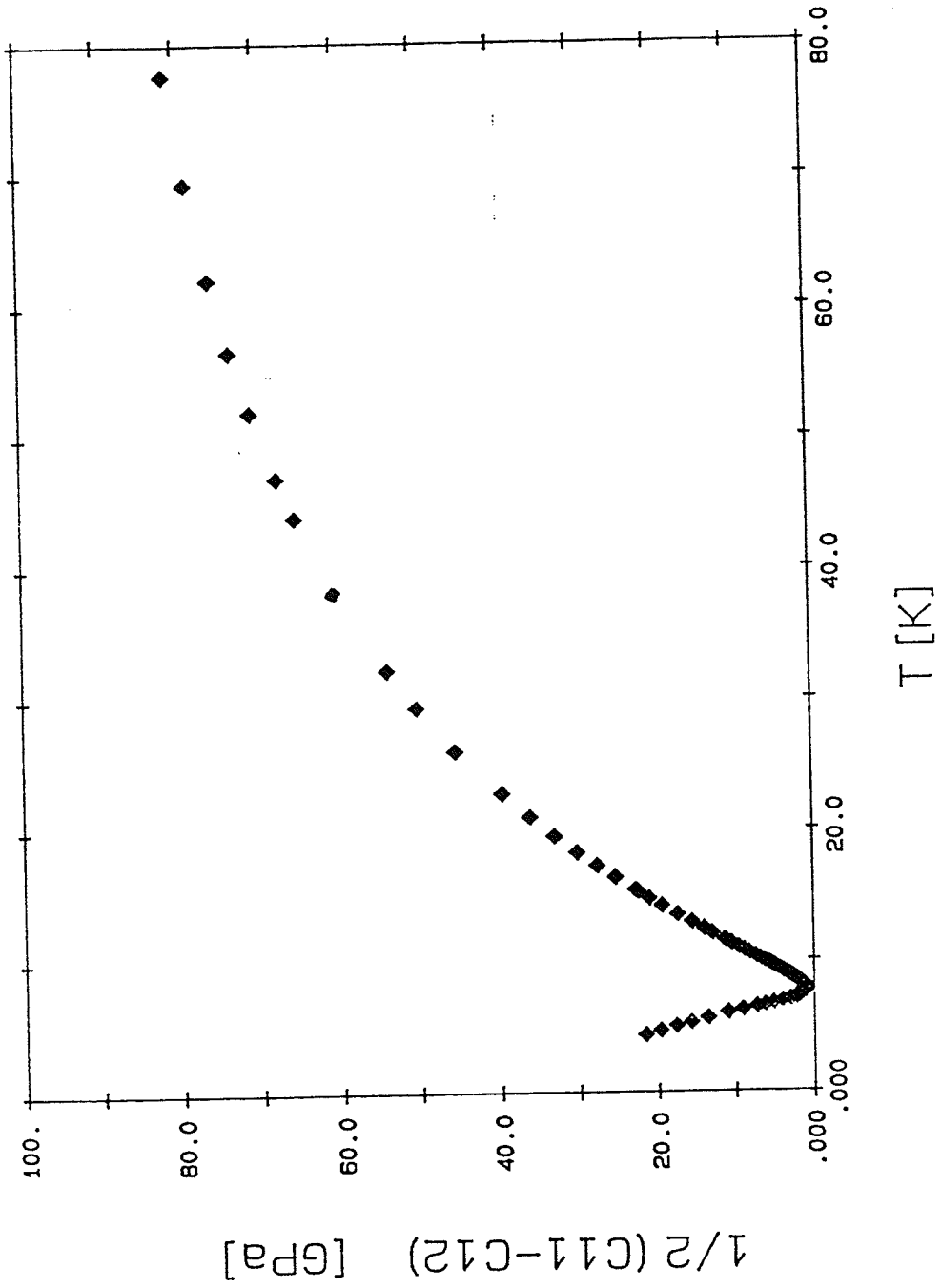


*Figure 4.15 Elastic constant* $1/2(c_{11}-c_{12})$ *calculated by subtracting* $1/2(c_{11}+c_{12})$ *from* $c_{11}$.

One possible explanation for the anomaly in figure 4.12 could be a misaligment of the [110] axis of the sample with respect to the normal to the polished faces of the sample. If the misaligment of the [110] axis were in the basal plane, the measured velocity would include a contribution that depends on $\frac{1}{2}(c_{11}-c_{12})$. To investigate this possibility, the orientation of the [110] axis was measured using the Laue back-reflection X-ray diffraction method ( for a review see Cullity (1956) ). The sample was bonded to a Z-cut quartz delay rod, the end face of which was known to be perpendicular to the quartz c axis to better than $1/2^{\circ}$, and the quartz rod was mounted on a triple axis goniometer. The orientation of the sample was compared to that of the quartz rod by taking a double X-ray picture; first the X-ray beam was focused on the sample and then, after a horizontal translation using the goniometer, a second exposure of the quartz was taken. The misaligment of the [110] axis of the sample relative to the quartz rod was found to be about $1.2^{\circ}$ ($\pm 0.5^{\circ}$) in the basal plane, with negligible misaligment in the a' c plane. Using the formulas in appendix II, the resulting correction to the measured elastic constants was then calculated and is shown in figure 4.16. This correction was found to be too small to explain the entire anomaly in $\frac{1}{2}(c_{11}+c_{12})+c_{66}$, being less than 20% of the observed variation in figure 4.12 ( If the misaligment were $2.5^{\circ}$, the variation within a few degrees of $T_D$ could be explained ,but not the total variation up to 30 K, as the temperature dependence of the

correction and the observed anomaly in $\frac{1}{2}(c_{11}+c_{12})+c_{66}$ are not identical ). Thus it appears that the anomaly in figure 4.12 is due to the temperature variation of $\frac{1}{2}(c_{11}+c_{12})$ near the transition. Even though the correction shown in figure 4.16 is quite small, it was subtracted from the $\frac{1}{2}(c_{11}+c_{12})+c_{66}$ data in order to calculate the temperature dependence of $\frac{1}{2}(c_{11}+c_{12})$ shown in figure 4.14. The softening of $\frac{1}{2}(c_{11}+c_{12})$ near the phase transition indicates that the coupling between the $A_{1g}$ strain and the electronic levels is not negligible, as assumed previously ( Page and Graham (1988) ). This coupling does not lower the crystal symmetry so that it can not lead to a phase transition. However, in systems such as these Dy compounds in which the two electronic levels are not exactly degenerate above $T_D$, coupling to an $A_{1g}$ mode can result in a change in the separation between the two nearly degenerate levels that is associated with a change in the magnitude of the c and a crystal axes. Although this type of interaction has been found to be the dominant one in cerium ethyl sulphate ( Graham and Page 1984 ), it is expected to be very weak in $DyAs_xV_{1-x}O_4$ since the $A_{1g}$ coupling was shown by Elliott *et al.* (1972) to be comparable to the weak $B_{2g}$ coupling and very much smaller than the dominant $B_{1g}$ coupling that drives the phase transition. We note that Elliott *et al.* (1972) were unable to measure the strength of all $A_{1g}$ couplings in pure $DyVO_4$ using Raman scattering and that our result for $\frac{1}{2}(c_{11}+c_{12})$ appears to be the first to demonstrate experimentally the presence of a linear Jahn-Teller coupling to this symmetric mode in the $DyAs_xV_{1-x}O_4$ system.

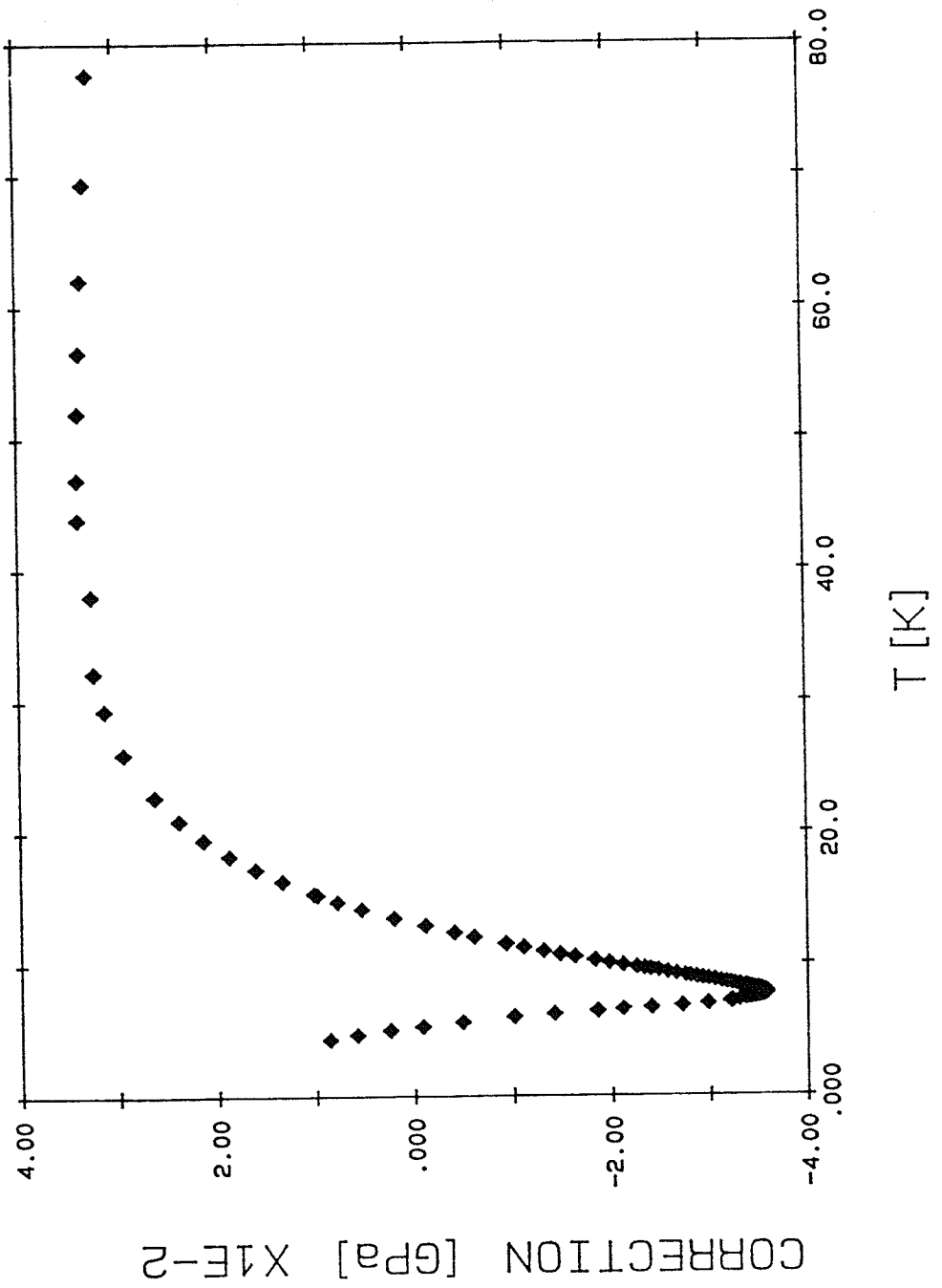


*Figure 4.16 Resulting misaligment correction versus Temperature (for 1.2° misaligment).*

The data for $\frac{1}{2}(c_{11}-c_{12})$ shown in figure 4.15 are consistent with the expected result that the soft mode elastic constant vanishes at the transition temperature $T_D$ in the static limit. However, even though the errors in measuring the variation of the elastic constant with temperature are small, the uncertainties in the absolute velocity measurements at room temperature are quite large, leading to a rather large uncertainties in the magnitude of $\frac{1}{2}(c_{11}-c_{12})$ at $T_D$ of ±1.2 GPa (see table 4.2). Thus to unambiguously establish that $\frac{1}{2}(c_{11}-c_{12})=0$ at $T_D$ using the procedure described above, the room temperature propagation time and the sample thickness must be measured more accurately. One approach that is showing promise for improving the accuracy of the absolute propagation time is measurements that exploit the improved signal-to-noise and timing resolution of a high-speed digital oscilloscope such as the Tektronix DSA 600; the use of signal averaging also allows propagation time data to be obtained at higher frequencies, where the signal would otherwise be buried in the noise.

Since the soft mode elastic constant $\frac{1}{2}(c_{11}-c_{12})$ is inversely proportion to the pseudo-spin susceptibility $\chi$, (*i.e* $\frac{1}{2}(c_{11}-c_{12}) \propto \chi^{-1} \propto t^{\gamma}$), the susceptibility critical exponent $\gamma$ can be determined from the data in figure 4.15 as follows. For the phase transition to occur, the static elastic constant must go to zero at $T_D$ implying that the observed minimum value of $\frac{1}{2}(c_{11}-c_{12})$ at $T_D$, $c_o=(0.96 \pm 1.2)$GPa, should

be subtracted from the data to give the variation of $\frac{1}{2}(c_{11}-c_{12})$ in the critical region. ( Note again that the uncertainties of ±1.2GPa is a systematic effect which accounts for a possible offset due to absolute velocity errors, not relative velocity errors near $T_D$ ).

The critical exponent $\gamma$ was determined by plotting the corrected data for $\frac{1}{2}(c_{11}-c_{12})$ ( *i.e.* the data in figure 4.16 minus $c_o$ ) *versus* the reduced temperature $t=(T-T_D)/T_D$ on a log-log plot as shown in figure 4.17. Good power law behavior is seen for $2x10^{-3}<t<7x10^{-2}$ with a slope $\gamma=1.78\pm0.07$.

Our result for $\gamma$ agrees with the theoretical predictions mentioned in § 2.5.1 namely: 1) The predictions of Monte Carlo simulations in which $\gamma$ was found to be 2.0±0.5 (Ogielski *et al.* (1986)) and 1.7±0.2 (Young *et al.* (1985)). 2) The prediction of dimensional reduction by 1 that postulates that $\gamma$ is equal to the value for a pure 2d nearest-neighbor Ising system (Onsager (1944)) for which $\gamma$ is 7/4. We should also mention the prediction of the scaling theory for RFIM developed by Bray and Moore (1985) in which the result for $\gamma$ in $2+\varepsilon$ dimensional systems gave $\gamma=0.5+1/\varepsilon$, which would give $\gamma=1.5$ for three dimensional system (*i.e.* $\varepsilon=1$). Although their prediction for $\gamma$ does not agree with ours, falling outside of our experimental uncertainties, their prediction that $\gamma$ increases in the presence of a random-field is consistent with our data and with previous measurements on this compound ( Graham *et al.* (1991)).

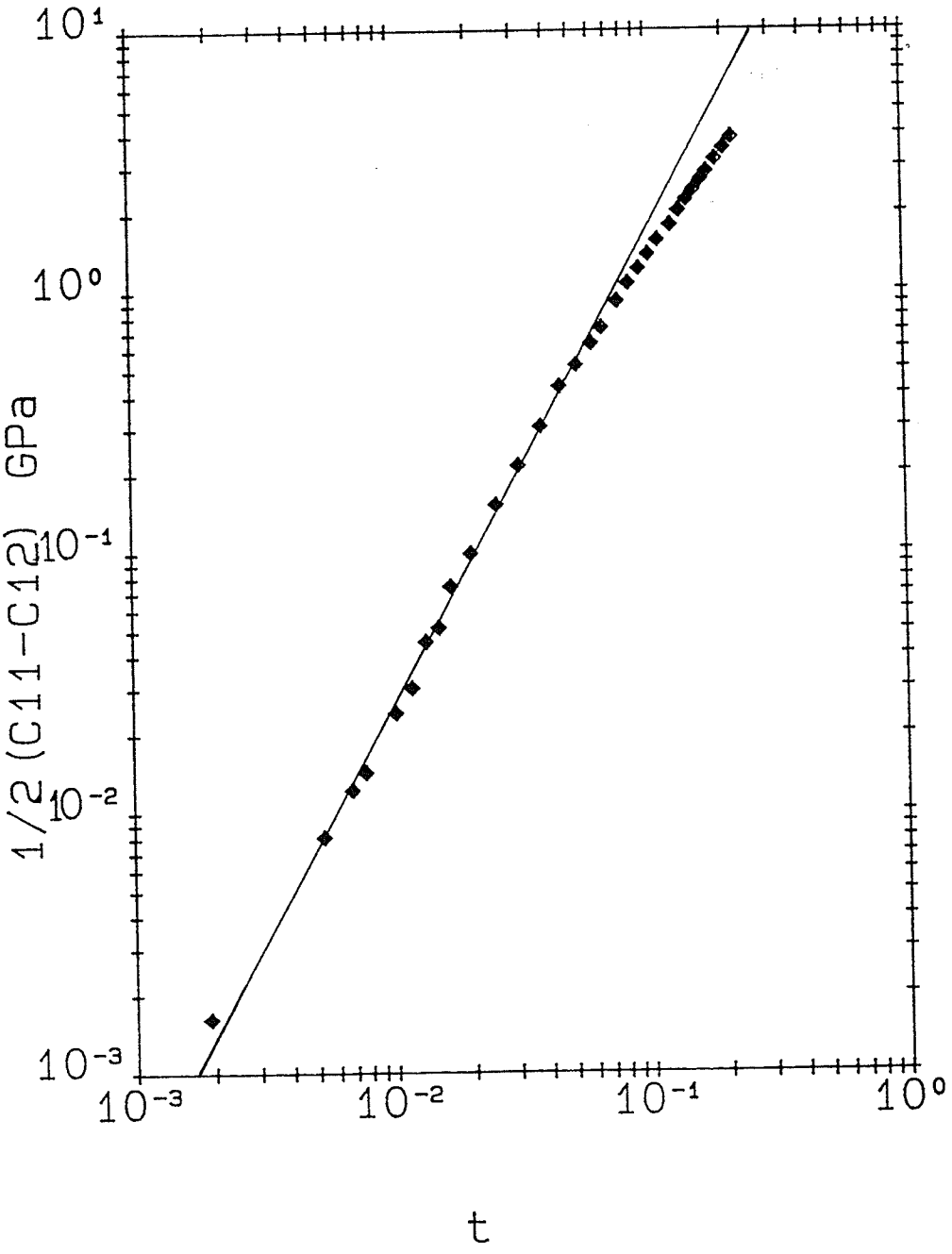


*Figure 4.17 Log-Log plot soft-mode elastic constant versus reduced temperature t for determination of the susceptibility critical exponent $\gamma$.*

The result for $\gamma$ is also consistent with two experimental results: 1) The result of measurements done on the same sample $DyAs_{0.15}V_{0.85}O_4$ and using an identical ultrasonic technique (Graham *et al.*(1991)), where $\frac{1}{2}(c_{11}-c_{12})$ was calculated directly without subtracting the weak temperature dependence of $\frac{1}{2}(c_{11}+c_{12})$ ( see § 5.2.1 ). Their result for $\gamma$, 1.80±0.06, is in complete agreement with ours. 2) The result of neutron scattering measurements (Belanger *et al.* (1985)) done on the dilute anti-ferromagnet $Fe_{0.6}Zn_{0.4}F_2$; their result for $\gamma$ is 1.75±0.20, which agrees with our result within the experimental uncertinities.

# CHAPTER FIVE CONCLUSIONS

Ultrasonic velocity measurements were successfully used to look for evidence of dynamic critical effects in the structural random-field system $DyAs_xV_{1-x}O_4$. We find that for strong random-field samples, dynamic effects are observed in the ultrasonic frequency range 25 MHz to 120 MHz as a result of the extreme slowing down of the critical fluctuations as the transition temperature is approached. Even though a much wider range of frequencies is needed to correctly model the behavior of the dynamic effects, it is clear now that such dynamic effects exist in this random-field Jahn-Teller compound, a fact that was not known before this work was begun.

Ultrasonic velocity measurements were also successfully used to investigate the static critical behavior of the soft mode elastic constant $\frac{1}{2}(c_{11}-c_{12})$ using a new approach in which $\frac{1}{2}(c_{11}-c_{12})$ was determined from independent measurements of both $c_{11}$ and the background contribution $\frac{1}{2}(c_{11}+c_{12})$. The elastic constant $\frac{1}{2}(c_{11}+c_{12})$ was found to exhibit a weak temperature dependence near the transition temperature, an effect which had not been investigated previously and which had been ignored in earlier work. The susceptibility critical exponent $\gamma$ for the random-field system $DyAs_xV_{1-x}O_4$ was found to be $1.78\pm0.07$ in a complete agreement with previous measurements done using a different approach. The power-law behavior from which $\gamma$ was determined was observed in the reduced temperature region $10^{-3}<t<10^{-1}$.

Future work will concentrate on: 1) improving the absolute propagation time measurements so that the soft mode elastic constant $\frac{1}{2}(c_{11}-c_{12})$ can be determined on absclute scale to greater precision at $T_D$ and 2) increasing the ultrasonic frequency range to further investigate the new dynamic effects reported in this thesis.

## APPENDIX I: DETERMINATION OF LONGITUDINAL AND SHEAR VELOCITIES OF INDIUM

The elastic constants of single-crystal indium have been measured as a function of temperature by Chandrasekar *et al.* (1961). To estimate the propagation delay through the thin indium layer used in our ultrasonic measurements, the average elastic constants for a polycrystaline sample must be calculated from the single crystal data. The usual approach is to take the average of rigorous upper and lower bounds for the bulk and shear moduli given by the Voigt and Reuss expressions (Anderson (1965)). The Voigt (1928) expressions for the bulk, and shear moduli, $K_v$ and $G_v$ ,(derived assuming constant strain in the crystallites) are written in terms of the elastic constants for indium as follows,

$$9K_v = 2c_{11} + c_{33} + 2(c_{12} + 2c_{13})$$
$$15G_v = 2c_{11} + c_{33} - (c_{12} + 2c_{13}) + 3(2c_{44} + c_{66}).$$

The corresponding Reuss (1929) expressions for $K_r$ and $G_r$ (derived assuming constant stress in the crystallites) are written in terms of the elastic compliances as,

$$1/K_r = (2s_{11} + s_{33}) + 2(s_{12} + 2s_{13})$$
$$15/G_r = 4(2s_{11} + s_{33}) - 4(s_{12} + 2s_{13}) + 3(2s_{44} + s_{66}).$$

Here the elastic compliances are defined in terms of the elastic constants as (Nye (1972)),

$$s_{11}=1/2\left( [c_{33}/C] + [ 1/(c_{11}- c_{12})]\right),$$

$$s_{12}=1/2\left([c_{33}/C] - [ 1/(c_{11}- c_{12})]\right),$$

$$s_{33}=(c_{11}+c_{12})/C,$$

$$s_{13}= - c_{13}/C,$$

$$s_{44}= 1/ c_{44},$$

$$s_{66}= 1/c_{66},$$

where $C \equiv (c_{11}+ c_{12})c_{33}- 2c_{13}^{2}.$

The polycrystalline bulk and shear moduli are given by (Anderson (1965))

$$K=\frac{1}{2}(K_v+K_r), \text{ and}$$
$$G=\frac{1}{2}(G_v+G_r).$$

The longitudinal velocity $v_L$ and shear velocity $v_s$ are related to the bulk and shear moduli as follows,

$$v_L = [(K + 3/4\ G)/\rho]^{1/2}$$

$$v_s = [\ G\ /\rho\ ]^{1/2}$$

The longitudinal and shear velocities are plotted as a function of temperature in figure AI.1.

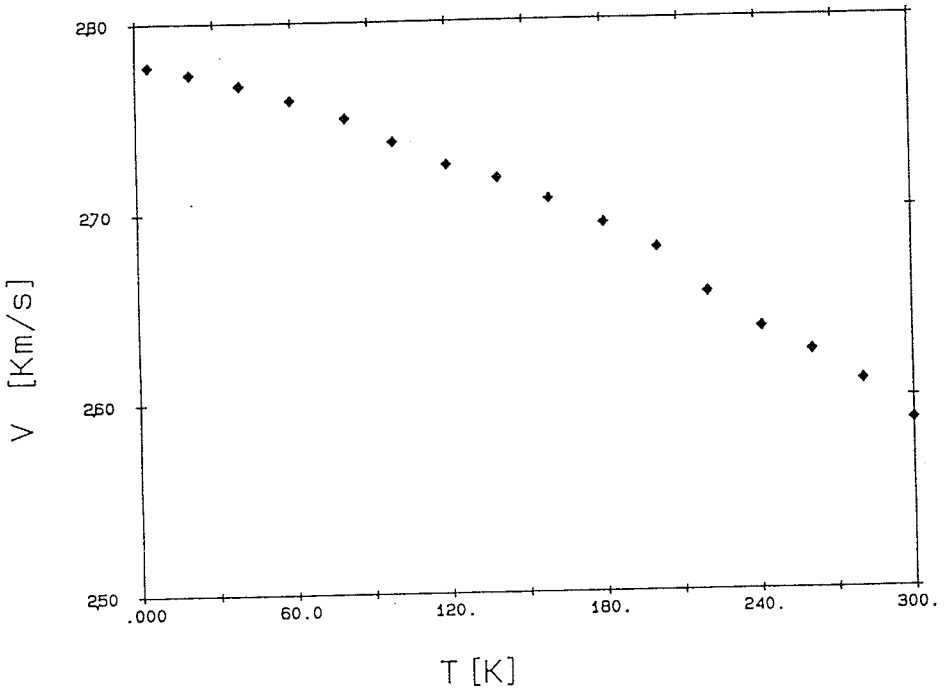


a)

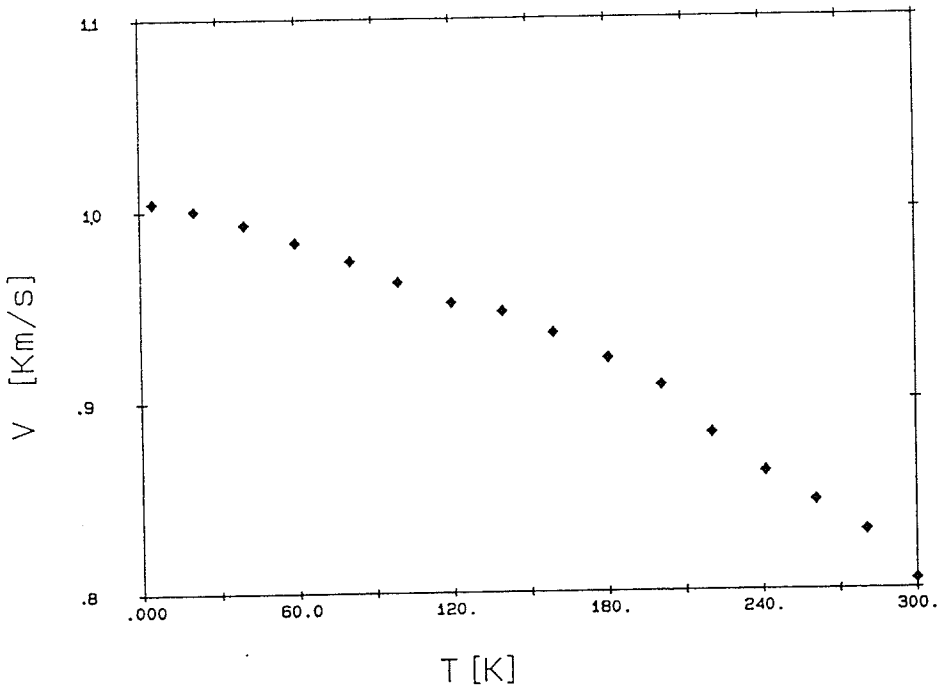


b)

Figure AI.1 Temperature variation of the ultrasonic velocity for indium a) longitudinal b) shear.

## APPENDIX II: SAMPLE MISALIGNMENT CORRECTIONS

In this appendix we calculate the relationship between the ultrasonic velocity and the elastic constants when the sample is misaligned by a small angel $\varepsilon$ with respect to the [110] direction in the basal (x-y) plane. The idea is to find periodic solutions to the equation of motion for plane waves propagating along the x′ direction (Neighbours *et al.* (1967))

$$\rho \frac{\partial^2 u'}{\partial t^2} = c'_{11} \frac{\partial^2 u'}{\partial x'^2} + c'_{16} \frac{\partial^2 v'}{\partial x'^2} + c'_{15} \frac{\partial^2 w'}{\partial x'^2} ,$$

$$\rho \frac{\partial^2 v'}{\partial t^2} = c'_{16} \frac{\partial^2 u'}{\partial x'^2} + c'_{66} \frac{\partial^2 v'}{\partial x'^2} + c'_{56} \frac{\partial^2 w'}{\partial x'^2} ,$$

$$\rho \frac{\partial^2 w'}{\partial t^2} = c'_{15} \frac{\partial^2 u'}{\partial x'^2} + c'_{56} \frac{\partial^2 v'}{\partial x'^2} + c'_{55} \frac{\partial^2 w'}{\partial x'^2} ,$$

where $\rho$ is the density , u, v, and w are the components of the displacement, $c'_{ij}$ are the elastic constants for a tetragonal I crystal (see Neighbours *et al.* (1967)), and x′ is the propagation direction.

For the impure longitudinal (transverse) mode of a misaligned sample the propagation direction is no longer parallel (perpendicular) to the displacement direction x. The propagation direction is now determined from the elastic constants, the most important of which is the anisotropy term $C_a = \frac{1}{2}(c_{11}-c_{12})-c_{66}$ ( which changes considerably as

the temperature is varied, since $\frac{1}{2}(c_{11}-c_{12})$ goes to zero at the phase transition). The sign of $C_a$ determines whether the propagation direction is tilted towards or away from the high symmetry direction. The tilt of the quasi-longitudinal (QL) mode direction away from the propagation direction x depends on the the ratio $C'_{16}/C'_{11}$, ( since $C'_{15}=C'_{56}=0$ for a basal plane misalignment ), and the tilt of the quasi-transverse (QT) mode direction away from being perpendicular to x' depends on $C'_{16}/C'_{66}$. For our purpose we only consider the QL case in which the tilt angle between the displacement and propagation direction is given by,

$$\theta_L = \tan^{-1}\frac{v'_o}{u'_o} = \tan^{-1}\left(\frac{\rho v_{QL}^2 - c'_{11}}{c'_{16}}\right),$$

Substituting for $c'_{11}$ and $c'_{16}$ in terms of the unprimed elastic constants and the angle $\delta$ between the propagation direction (x') of the impure mode and [110], we obtain

$$\theta_L = \tan^{-1}\left(\tan 2\delta_L \frac{C_a}{C_d - C_a}\right),$$

$$\cong 2\delta_L \frac{C_a}{C_d - C_a} \quad \text{for small } \delta.$$

For a fixed $\delta_L$, $\theta_L$ changes sign as a function of temperature. Relative to x', $\theta_L<0$ when the displacement is tilted towards [110] (T *near* $T_D$), and and $\theta_L>0$ when the displacement is tilted away from [110] (T *far from*

$T_D$). In ultrasonic experiments the displacement direction (perpendicular to the polished sample faces) is fixed relative to the crystal axis, so that the quantity $\varepsilon_L=\theta_L+\delta_L$ is fixed, and

$$\varepsilon_L=\theta_L\left[1+\frac{C_d-C_a}{2C_a}\right]=\theta_L\left[\frac{c_{11}-c_{66}}{2\,C_a}\right],\ \text{or}$$

$$\varepsilon_L=\delta_L\left[1+\frac{2C_a}{C_d-C_a}\right]=\delta_L\left[\frac{c_{11}-c_{66}}{c_{12}+c_{66}}\right],$$

Thus the angle between the propagation direction and the [110] direction is

$$\delta=\frac{\varepsilon_L(C_d-C_a)}{C_d+C_a}.$$

The correction for the QL mode velocity due to the misalignment can be determined from the following solution of the equation of motion

$$\rho v^2=\frac{1}{2}(c_{11}+c_{12})+c_{66}+4\delta^2\frac{C_d\,C_a}{C_d-C_a},$$

Substituting for $\delta$ we get

$$\rho v_L^2=\frac{1}{2}(c_{11}+c_{12})+c_{66}+4\varepsilon_L^2\,C_dC_a\left(\frac{C_d-C_a}{[C_d+C_a]^2}\right),$$

Calculations done using the measured values of $c_{11}$, $\frac{1}{2}(c_{11}+c_{12})$, $\frac{1}{2}(c_{11}-c_{12})$ and $c_{66}$ are shown in figure 4.16.

# REFERENCES


Aharony, A., Imry, Y. and Ma, S. 1976: *Phys. Rev. Lett.* **37,** 1364

Anderson, O. L. 1965: in Physical Acoustics, Vol III, Part **B**, (ed. by W.P. Mason) ( Academic Press, New York ) pp 43-97.

Bleaney, B.I. and Bleaney, B.1976: Electricity and Magnetism 3rd ed. (Oxford University Press, London ). sec. 9.5.

Bray,A.J. and Moore, M.A. 1985: *J. Phys. C* **18,** L927.

Chandrasekhar, B. S. and Ryne, J. A. 1961: *Phys. Rev.* **124**, 1011.

Ashcroft, N. W. and Mermin, N. D.1976: Solid State Physics, (Holt, Reinhart, and Winston, Inc., New York, )

Belanger, D. P., King, A. R., Jaccarino, V. and Nicklow, R. M. 1987:*Phys. Rev.* **B 59** 930.

Belanger, D. P., King, A. R., and Jaccarino, V. 1985: *Phys. Rev.* **B 31** 4538.

Belanger, D. P., King, A. R., Ferreira, I. B., and Jaccarino, V. 1988: *Phys. Rev.* **B 37** 219.

Callaway, J. 1956: Quantum Theory of Solids, (Academic Press, London& New York) (19 ).

Elliott, R. J., Harley, R.T., Hayes, W., and Smith, S. R. P. 1972: *Proc. Roy. Soc. London A* **328,** 217.

Fisher, D. S. 1986: *Phys. Rev. Lett.* **56**, 416.

Gehring, G. A. and Gehring, K. A. 1975: *Rep. Prog. Phys.* **38**, 1.

Glynn, T.J. Harley, R.T. and Macfarlane, R.M. 1977: *J. Phys. C* **10,** 2973.

Graham, J. T. 1984: *"Ultrasonic Investigation of the Jahn-Teller Effect in Cerium Ethyl Sulphate"* MSc. Thesis. Queen's University, Kingston, Ontario Canada.

Graham, J. T. 1990: *"An Experimental Investigation Into The Random-Field Effect in the Mixed Jahn-Teller System* $DyAs_xV_{1-x}O_4$ " PhD Thesis Queen's University, Kingston, Ontario Canada.

Graham, J. T., Page, J.H., and Talyor, D.R. 1991: To be published.

Gorodetsky, G. and Lüthi, B. 1971: *Solid State Comm.* **9** 2157.

Huse, D.A. and Henley, C.L. 1985: *Phys Rev. Lett.* **54,** 2708.

Jahn, H. A. and Teller, E. 1937: *Proc. Roy. Soc.* **A 161**, 220.

Jaccarino, E. and King, A. R. 1988: *J de Physique* C8-1209.

Jaccarino, V. Nash, A. E. and King, A. R. 1991: *Phys. Rev.* **B 43**, 1272.

Kasten, A., Kahle, H. G. and Klofer, P. 1984: *Solid State Commun.* **52,** 725.

Kasten, A. 1980: *Z. Phys.* **B 38**, 65

Kittel, C. 1966:, Introduction to Solid State Physics, 3rd ed. (John Wiley & sons New York).

King, A. R., Mydosh, J. A. and Jaccarino, V. 1986: *Phys. Rev. Lett.* **56,** 2525.

Melcher, R.L. and Scott, B.A. 1972: *Phys. Rev. Lett.* **28,** 607

Novakovic, L.1957: The Pseudo-spin in Magnetism and Ferroelectricity, (Pergamon Press. Oxford& New York).

Neighbours, J. H. and Schacher, G. E. 1967: *J. Appl. Phys.* **38**, 5366.

Nye, J.F.1957: Physical Properties of Crystals, ( University Press. Oxford.

Ogielski, A.T., and Huse, D.A. 1986: *Phys. Rev. Lett.* **56**, 1298.

Pachet, N. G. 1990: *"Ultrasonic Velocity and Attenuation in a Glass-Bead Percolation System "*, MSc. Thesis, University of Manitoba.

Page J. H. 1976: *" Microwave Ultrasonic investigatio at Low Temperatures"*, D.Phil. thesis, University of Oxford, Oxford.

Page J. H. and Rosenberg, H. M.1977: *J. Phys.*, **C 10**. 1817.

Page, J.T, Taylor, D.R. and Smith, S.R.P. 1984: *J. Phys. C* **17,** 51.

Page J. H. and Graham, J.T 1988: *J. de Physique* **49** C8-1227.

Page J. H., Smith, S.R.P., Taylor D.R., and Harley, R.T. 1975: *J. Phys.* C **12**, L875.

Smart, J. S. 1966: Effective Field Theory of Magnetism (W. B. Saunders Company, Philadelphia & London).

Taylor, D. R., Zwartz, E., and Page, J. H. 1986: *J. Mag. and Mag. Magnetic Materials.* Part I, 57.

Villain, J. 1985: *J. Physique* **46**, 1843.

Waterman, P. C. 1959: *Phys. Rev.* **113**, 1240.